General Disclaimer

One or more of the Following Statements may affect this Document

- This document has been reproduced from the best copy furnished by the organizational source. It is being released in the interest of making available as much information as possible.

- This document may contain data, which exceeds the sheet parameters. It was furnished in this condition by the organizational source and is the best copy available.

- This document may contain tone-on-tone or color graphs, charts and/or pictures, which have been reproduced in black and white.

- This document is paginated as submitted by the original source.

- Portions of this document are not fully legible due to the historical nature of some of the material. However, it is the best reproduction available from the original submission.

NATIONAL AERONAUTICS AND SPACE ADMINISTRATION

Technical Memorandum 33-731

Experimental Aerodynamic Characteristics of Vehicles Traveling in Tubes

Donald W. Kurtz

Bain Dayman, Jr.

JET PROPULSION LABORATORY

CALIFORNIA INSTITUTE OF TECHNOLOGY

PASADENA, CALIFORNIA

July 15, 1975

PREFACE

The work described in this report was performed by the Applied Mechanics Division of the Jet Propulsion Laboratory.

CONTENTS

I.	Introduction		1
II.	Simplified Steady-State Theoretical Model		2
	A.	Vehicle Drag	2
	B.	Tube Flow Velocity	9
III.	Test Procedure/Data Acquisition		12
	A.	Facilities	12
	B.	Models	13
	C.	Measurements	14
	D.	Data Reduction	14
IV.	Data Presentation		16
	A.	Drag	16
	B.	Flow Velocity in Tube	18
	C.	Momentum Coefficients	20
	D.	Friction Factors	22
V.	Analysis		24
	A.	Elements of Aerodynamic Drag	24
	B.	Pressure Signature Characteristics	25
	C.	Drag Inferred From Pressure Signature	26
	D.	Sensitivity of Predicted Vehicle Drag Coefficient to Variations in Constants	27
VI.	Unsteady Aerodynamics		28
	A.	Slug Theory	29
	B.	System Power Requirements	32
VII.	Recommendations		34
VIII.	Summary		35

Definition of Symbols 36

References 38

Bibliography 38

TABLES

1. VICS run summary 40
2. Nominal momentum coefficient values 41
3. Percent variation in C_D for a 20% variation in the C constants 41

FIGURES

1. VICS-120 facility under construction 42
2. Models of vehicles tested 43
3. Effect of Reynolds number on drag coefficient (all walls smooth, L/D = 630, ℓ/d = 15) 44
4. Effect of blockage ratio on drag coefficient ($R_d = 10^6$, ℓ/d = 15) 44
5. Effect of vehicle length on drag coefficient ($R_d = 10^6$, smooth tube wall, L/D = 630) 45
6. Effect of tube length on drag coefficient ($R_d = 10^6$, all walls smooth, ℓ/d = 15) 45
7. Effect of vehicle nose and base shape on drag coefficient ($R_d = 3 \times 10^4$, all walls smooth, L/D = 290, ℓ/d = 15) 46
8. Effect of eccentricity on drag coefficient ($R_d = 2\text{-}1/2 \times 10^4$, all walls smooth, L/D = 404, ℓ/d = 15) 47
9. Effect of Reynolds number on velocity ratio of flow in tube (all walls smooth, L/D = 630, ℓ/d = 15) 47
10. Effect of vehicle blockage ratio on velocity ratio of flow in tube ($R_d = 10^6$, smooth model wall, ℓ/d = 15) 48
11. Effect of tube length on velocity ratio of flow in tube ($R_d = 10^6$, all walls smooth, ℓ/d = 15) 48
12. Effect of vehicle blockage ratio on momentum coefficients ($R_d = 10^6$, smooth tube wall L/D = 630 and ∞) 49

13. Effect of Reynolds number on nose momentum coefficient (smooth tube wall, L/D = 630). 50

14. Effect of Reynolds number on base momentum coefficient (smooth tube wall, L/D = 630). 50

15. Effect of Reynolds number on wake momentum coefficient (smooth tube wall, L/D = 630). 51

16. Ratio of downstream to upstream pipe flow friction factors (smooth tube wall). 51

17. Effect of annular Reynolds number on annular friction factor in a smooth wall tube (L/D = 630, ℓ/d = 15) 52

18. Effect of vehicle blockage ratio on annular friction factor (annular Reynolds number = $1/2 \times 10^6$, smooth model wall, ℓ/d = 15) 53

19. Effect of annular Reynolds number on annular friction factor in a ribbed tube (L/D = 845, ℓ/d = 15). 54

20. Elements of aerodynamic drag ($R_d = 10^6$, all walls smooth, L/D = 630, ℓ/d = 15). 55

21. Typical pressure signatures ($R_d \sim 3 \times 10^6$, all walls smooth, L/D = 630, ℓ/d = 15). 56

22. Schematic of a typical pressure signature 56

23. Non-dimensionalized characteristics of typical pressure signatures 57

24. Comparison of aerodynamic drag inferred from pressure signature with that directly obtained from model weight. 58

25. Aerodynamic and rolling friction power requirement as a function of train velocity 59

26. Unsteady train velocity schedule, resulting air flow velocity in tunnel and instantaneous train drag coefficient 60

27. Component parts of constant unsteady power requirement for train in a smooth tunnel 61

28. Component parts of constant unsteady power requirement for train in a ribbed tunnel 61

ABSTRACT

Experimental investigations on the aerodynamic characteristics of trains traveling in tunnels have been carried out in the Vehicles In Confined Spaces (VICS) 70 and 120 small-scale test facilities. The purpose of these investigations was to develop sufficient understanding of the scaling considerations of subway train system aerodynamics that, with the use of theoretical models, adequate predictions could be made for full-scale systems. A considerable amount of high-quality data was obtained during the 2 years of testing.

A simplified theoretical model for a vehicle traveling through an unvented tube under equilibrium incompressible conditions was used to guide the test program, reduce the data, and determine the self-consistency of the results. The results were then used to establish values for the arbitrary coefficients in the theoretical model. Substantial progress was made in understanding the aerodynamic characteristics of vehicles traveling in tubes as exemplified by the good agreement of the theoretical model predictions with the experimental data throughout the Reynolds number range (three orders of magnitude, up to that for an actual full-scale system) and the many geometric variables tested.

I. INTRODUCTION

In recognition of the influence aerodynamics has on the design and operation of intra-urban rapid transit subway-train systems, an experimental test program was initiated at the Jet Propulsion Laboratory to develop an understanding of the basic aerodynamic characteristics of vehicles traveling in tubes. As train speeds increase and the tunnel area relative to the frontal area of the train decreases, aerodynamics plays an increasingly important role in the design and operation of the system. The aerodynamic drag increases with the increasing train velocities and blockage ratio; hence, the power requirements for propulsion, subsequent heat rejection from the train into the system, air flow velocities, and pressure pulses also increase.

Both experimental and theoretical work on the aerodynamics of tube-vehicle systems has been going on for a number of years in many countries throughout the world (Ref. 1). However, the development of the theoretical understanding of the aerodynamic characteristics of such systems has not had the advantage of thorough experimental studies. Hence, the emphasis of this report is on the presentation of the experimental data recently obtained at JPL. The investigation was performed in several small-scale facilities, specially constructed for these studies, in which the vehicles moved with respect to the tube under equilibrium conditions up to full-scale Reynolds numbers.

The main purposes of these studies were to obtain information necessary for the development of a near-field theoretical model and to provide verification of the aerodynamic scaling laws which are fundamental inputs to the Subway Environmental Design Handbook (Ref. 2). The handbook is a part of the Ventilation and Environmental Control in Subway Rapid Transit Systems project* directed by the Transit Development Corporation for the Urban Mass Transportation Administration of the Department of Transportation. Experimental studies covering a wide range of geometric variables pertinent to intra-urban subway-train transportation systems were carried

*This project was initiated under the direction of the Institute for Rapid Transit.

out from low Reynolds numbers (at which such tests are usually conducted) up to virtually maximum full-scale Reynolds numbers.

Two hundred and forty-four runs were made in the VICS-120 facility, completely reduced, and analyzed to varying degrees. These runs complement the 32 applicable runs made in the VICS-70 facility. Blockage ratio, model length, nose and tail shape, model wall roughness, model porosity, model eccentricity in tube, tube length, tube wall roughness, and nonequilibrium effects were all investigated over a range of Reynolds numbers. A summary of the pertinent runs is presented in Table 1.

II. SIMPLIFIED STEADY-STATE THEORETICAL MODEL

In order to guide an experimental program of this type and analyze the results, a theoretical model which describes the near-field aerodynamic characteristics of a vehicle traveling in a tube was necessary. A basic understanding of tube-vehicle aerodynamic characteristics can be obtained by the proper application of normal pipe flow laws and momentum considerations. The formulation of this simplified theoretical model is based on these two principles. In order to further simplify the formulation, the following assumptions are made:

(1) Incompressible flow

(2) Steady-state equilibrium conditions

(3) Single, unvented, constant-diameter tube

(4) Single vehicle

A. VEHICLE DRAG

The vehicle drag is composed of several distinct but related elements, as follows:

$$D = D_N + D_{SF} + D_{PD} + D_B$$

where

D_N = form drag due to Bernoulli pressure drop over nose of vehicle (assumes ideal 1-dim. inviscid flow)

D_{SF} = drag due to viscous flow along cylindrical portion of vehicle

D_{PD} = pressure drop drag due to skin friction force on both vehicle cylindrical wall and tube wall immediately surrounding vehicle

D_B = base drag due to decrease in pressure as flow expands over base of vehicle

C_D = $D/(1/2\,\rho v^2 a)$, where v is velocity of vehicle relative to tube wall, and a is frontal area of vehicle

1. Form Drag D_N

From Bernoulli considerations assuming one-dimensional inviscid flow, based upon the flow velocity relative to the vehicle (see Sketch 1):

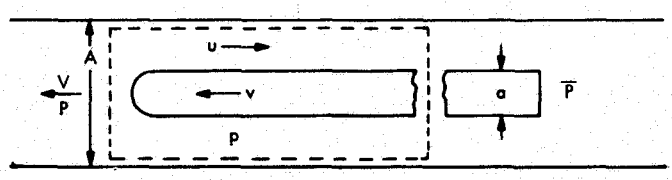

Sketch 1

$$P + \frac{1}{2}\rho(v - V)^2 = p + \frac{1}{2}\rho(v + u)^2$$

By continuity,

$$\frac{u}{v} = \frac{\sigma - \beta}{1 - \sigma}$$

By combining the preceding expressions,

$$P - p = C_1\sigma(2 - \sigma)\left(\frac{1 - \beta}{1 - \sigma}\right)^2 \frac{1}{2}\rho v^2 \qquad (2\text{-}1)$$

where an arbitrary constant C_1 is included since the experimental pressure drop may differ from the theoretical one.

The momentum theorem may now be applied to the dashed area in order to obtain the form drag of a semi-infinite cylinder in a pipe. (Velocities are relative to the vehicle and viscous forces are neglected.)

$$D_N = A(P - p) + A\rho(v - V)^2 - (A - a)\rho(V + u)^2 \qquad (2\text{-}2)$$

Substituting for (P - p) above and using the expressions for u and A yields the form drag coefficient

$$C_{D_N} = \left(\frac{1 - \beta}{1 - \sigma}\right)^2 [\sigma(2 - C_1) + 2(C_1 - 1)]$$

where

$$C_{D_N} = \frac{D_N}{1/2\rho v^2 a} \qquad (2\text{-}3)$$

2. Skin Friction Drag D_{SF}

In order to obtain a reasonable approximation of the vehicle wall skin friction drag due to flow in the annular region, a two-dimensional channel flow solution is satisfactory (see Sketch 2).

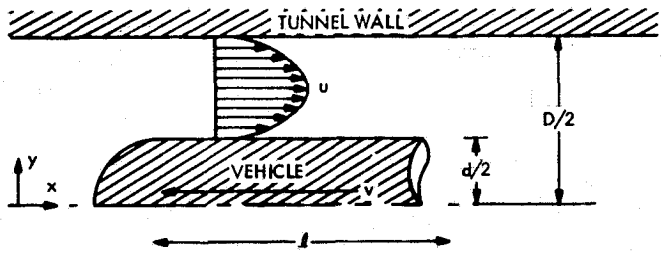

Sketch 2

Now,

$$-\frac{dp}{dx} = \mu \frac{d^2u}{dy^2} \tag{2-4}$$

Integration yields

$$\mu \frac{du}{dy} = \frac{dp}{dx} y + \text{constant}$$

Since $\tau = \mu\,(du/dy)$, and the boundary condition is imposed that $du/dy = 0$ when $y = (D + d)/4$, the shear stress at the vehicle wall is

$$\tau_w = \frac{dp}{dx} \frac{D - d}{4} \text{ or } \tau_w = \frac{\Delta P}{\ell} \frac{D - d}{4} \tag{2-5}$$

Now, the well known Darcy-Weisbach equation for pipe flow around the vehicle may be written

$$\frac{\Delta P}{\ell} = \frac{f_V}{D - d} \frac{\rho}{2} (v + u)^2 \tag{2-6}$$

Proper substitution of ΔP and u into Eq. (2-5) yields

$$\tau_w = \frac{f_V}{8} \rho v^2 \left(\frac{1 - \beta}{1 - \sigma} \right)^2 \tag{2-7}$$

The drag force due to skin friction is $D_{SF} = \tau_w \pi d \ell$, and the drag coefficient is just

$$C_{D_{SF}} = \frac{D_{SF}}{1/2 \rho v^2 a}$$

where $a = \pi d^2/4$. So,

$$C_{D_{SF}} = f_V \frac{\ell}{d} \left(\frac{1 - \beta}{1 - \sigma} \right)^2 \tag{2-8}$$

3. Pressure Drop Drag D_{PD}

The use of pipe flow principles in the annular region between the vehicle and the tube is complicated since the bulk flow velocity relative to the vehicle wall is different from that relative to the tube wall. Rather than base the pipe flow friction on just one of the relative velocities (or some arbitrary average velocity), the pipe flow principles can be independently applied to each wall (vehicle and tube). This is accomplished by using the basic annular pipe flow friction factor based on the relative velocity along one of the walls, and then decreasing that pressure drop by the ratio of that wall area to the total wall area. The total pressure drop is then

$$\Delta p = \Delta p_V + \Delta p_T \tag{2-9}$$

where

$$\Delta p_V = f_V \frac{\ell}{D - d} \frac{\rho}{2} (v + u)^2 \frac{\sqrt{\sigma}}{1 + \sqrt{\sigma}}$$

where $\sqrt{\sigma}/(1 + \sqrt{\sigma})$ is just the vehicle wall area ratio and

$$\Delta p_T = f_T \frac{\ell}{D - d} \frac{1}{2} \rho u^2 \left(1 - \frac{\sqrt{\sigma}}{1 + \sqrt{\sigma}} \right)$$

By using the relations already established for d and u, the total pressure drop along the length of the vehicle due to tube and vehicle wall friction can be expressed as

$$\Delta p = f_V \frac{\ell}{d} \frac{\sigma}{1-\sigma} \left(\frac{1-\beta}{1-\sigma}\right)^2 \frac{1}{2}\rho v^2 \pm f_T \frac{\ell}{d} \frac{\sqrt{\sigma}}{1-\sigma} \left(\frac{\sigma-\beta}{1-\sigma}\right)^2 \frac{1}{2}\rho v^2 \qquad (2\text{-}10)$$

where the + term is used for $\sigma > \beta$, and the - term for $\sigma < \beta$.

This pressure drop acts on the base area to give a drag force. By combining the terms and converting to a drag coefficient, we get

$$C_{D_{PD}} = \frac{\ell}{d} \frac{1}{(1-\sigma)^3} f_V \sigma (1-\beta)^2 \pm f_T \sqrt{\sigma} (\sigma-\beta)^2 \qquad (2\text{-}11)$$

The Reynolds number for determining the values for f_V and f_T can also be based upon the bulk flow velocity relative to the wall being considered, giving

$$R_V = \frac{\rho(v+u)(D-d)}{\mu}$$

and

$$R_T = \frac{\rho u(D-d)}{\mu}$$

where (D - d) is the hydraulic diameter.

By using the already developed expressions for u and d, we get

$$R_V = \frac{\rho u D}{\mu} \frac{1-\beta}{1+\sqrt{\sigma}}$$

$$R_T = \frac{\rho u D}{\mu} \left| \frac{\sigma\beta}{1+\sqrt{\sigma}} \right|$$

4. Base Drag D_B

A sudden expansion and resulting pressure drop drag increment occur at the vehicle base. The pressure drop may be determined by writing the continuity, energy, and momentum equations in that region. The solution may be simplified, however, if it is expressed only as a function of flow velocity in the annular region relative to the vehicle,

$$\Delta P_B = C_2 \frac{1}{2}\rho v^2 \left(\frac{1 - \beta}{1 - \sigma}\right)^2 \tag{2-12}$$

where C_2 is a function of the blockage ratio.

The base drag coefficient, then, is just

$$C_{D_B} = \frac{\Delta P_B a}{1/2 \rho v^2 a}$$

or

$$C_{D_B} = C_2 \left(\frac{1 - \beta}{1 - \sigma}\right)^2 \tag{2-13}$$

5. Vehicle Total Drag Coefficient

The resulting total drag coefficient for the vehicle is the summation of the four sources of drag (Eqs. 2-3, 2-8, 2-11, and 2-13). Therefore,

$$C_D = C_{D_N} + C_{D_{SF}} + C_{D_{PD}} + C_{D_B}$$

or

$$C_D = \left[f_v \frac{\ell}{d} + C_2 + \sigma(2 - C_1) + 2(C_1 - 1)\right] \left(\frac{1 - \beta}{1 - \sigma}\right)^2$$

$$+ \frac{\ell}{d} \frac{1}{(1 - \sigma)^3} [f_V \sigma (1 - \beta)^2 \pm f_T \sqrt{\sigma(\sigma - \beta)^2}] \tag{2-14}$$

where + is for $\sigma > \beta$ and - is for $\sigma < \beta$.

B. TUBE FLOW VELOCITY

In order to determine the ratio of the bulk flow velocity ratio (β) in the tube away from the vehicle, it is first necessary to determine the various pressure gradients and steps along the entire length of the tube, including the region occupied by the vehicle. The diagram (shown in Sketch 3) divides the tube into six regions, with the seventh (or end) region taking care of natural or augmented end losses for both ends.

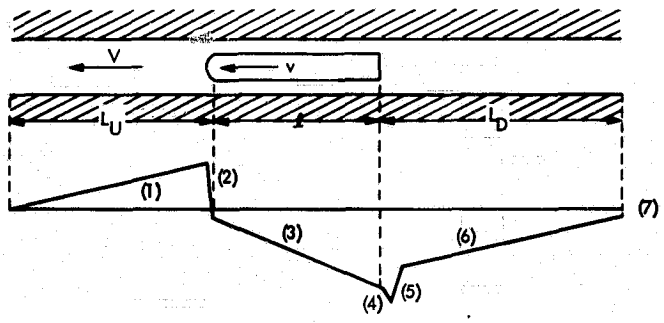

Sketch 3

1. Region 1: Pressure Gradient Along Tube Upstream of Vehicle

This pressure gradient is due to the normal flow through a tube as predicted by the usual pipe flow friction factor considerations. The expression is

$$\Delta P_1 = f_U \frac{L_U}{D} \frac{1}{2} \rho v^2 \beta^2 \tag{2-15}$$

2. Region 6: Pressure Gradient Along Tube Downstream of Vehicle

Since the form of the pressure gradient is assumed to be identical to that for Region 1, it is convenient to discuss it at this time. The main difference between the flows in Regions 1 and 6 is due to the vehicle wake effect on the velocity profile in Region 6. Because of the wake effect, it is likely that the friction factor will differ from the normal pipe flow friction factor of Region 1. Hence,

$$\Delta P_6 = f_D \frac{L_D}{D} \frac{1}{2} \rho v^2 \beta^2 \tag{2-16}$$

The length L_D really should not include Regions 4 and 5, but this is neglected.

3. Region 2: Pressure Drop Over Nose of Vehicle

The Bernoulli pressure drop over the nose of the vehicle, with the factor C_1 to correct for the possible difference between theory and experiment, is

$$\Delta P_2 = C_1\sigma(2 - \sigma)\left(\frac{1-\beta}{1-\sigma}\right)^2 \frac{1}{2}\rho v^2 \tag{2-17}$$

and is identical to Eq. (2-1).

4. Region 3: Pressure Gradient Along Vehicle

The pressure drop in the annular region due to the friction on both the vehicle and the tube is

$$\Delta p_3 = -\frac{\ell}{d}\frac{1}{(1-\sigma)^3}[f_V\sigma(1-\beta)^2 \pm f_T\sqrt{\sigma}(\sigma - \beta)^2]\frac{1}{2}\rho v^2 \tag{2-18}$$

and is identical to Eq. (2-10).

5. Region 4: Pressure Drop at Vehicle Base

The pressure drop at the base of the vehicle, due to the sudden flow expansion, is

$$\Delta p_4 = -C_2\left(\frac{1-\beta}{1-\sigma}\right)^2 \frac{1}{2}\rho v^2 \tag{2-19}$$

and is the same as Eq. (2-12).

6. Region 5: Pressure Recovery Aft of Vehicle Base

The pressure rise in Region 5 can be considered to be a recovery of the original pressure drop in Region 2 less the loss due to the vehicle form drag. Assuming inviscid flow, and using the bulk flow velocity in the tube relative to the vehicle, this pressure rise can be determined as follows. By applying the momentum theorem to a region encompassing the entire vehicle, we get

$$P_U A + A\rho(v - V)^2 = P_D A + A\rho(v - V)^2 + D_N \tag{2-20}$$

or

$$(P_U - P_D) = \frac{D_N}{A}$$

where D_N is defined by Eq. (2-2).

What is actually desired is the pressure rise $(P_D - p)$, at the base, which is equivalent to

$$\Delta P_5 = (P_U - p) - (P_U - P_D) \tag{2-21}$$

but $(P_U - p)$ is just ΔP_2; therefore,

$$\Delta P_5 = C_3 \frac{\sigma}{(1 - \sigma)}(1 - \beta)^2 \rho v^2 \tag{2-22}$$

where C_3 is an arbitrary constant which is ideally unity. Experimental results, however, indicate that this is not always the case.

7. Region 7: Tube Entrance Pressure Drop

The pressure drop at the tube ends can be lumped into a drop at only the entrance end. It can be written in the form

$$\Delta P_7 = \frac{1}{2}\rho v^2 \beta^2 \alpha \tag{2-23}$$

where α is the loss coefficient.

For the case of a simple tube with both ends open, the value of α was experimentally found to be approximately -1.7. If a restriction of some sort is at the tube end, the absolute value of α will be increased. Should some means of flow augmentation be used, the sign as well as the magnitude of α will change.

8. Regions 1 through 7: Complete Pressure Balance Equation

The pressure equation for the tube can now be written, and by solving this equation, the value of β (ratio of the bulk tube flow velocity to the vehicle velocity) can be determined using

$$\underbrace{\Delta P_7}_{\text{Normally negative value}} = \underbrace{\Delta P_1 + \Delta P_6 + \Delta P_5}_{\text{Positive values}} + \underbrace{\Delta P_2 + \Delta P_3 + \Delta P_4}_{\text{Negative values}} \tag{2-24}$$

$$\alpha = f_U \frac{L_U}{D} + f_D \frac{L_D}{D} - \frac{\sigma}{\beta^2}\left(\frac{1-\beta}{1-\sigma}\right)^2 \left[C_1(2-\sigma) + \frac{1}{\sigma}C_2 - 2C_3(1-\sigma)\right]$$

$$- \frac{\ell}{d} \frac{1}{\beta^2(1-\sigma)^3} \left[f_V \sigma (1-\beta)^2 \pm f_T \sqrt{\sigma}\,(\sigma-\beta)^2\right] \tag{2-25}$$

where the + sign is used for $\sigma > \beta$ and the - sign is used for $\sigma < \beta$.

In summary, in order to calculate the steady-state incompressible drag coefficient of a vehicle traveling in a single, unvented tube, it is first necessary to determine β from the pressure balance equation (Eq. 2-25). An iterative solution is necessary, since the friction factors (f) are based upon the appropriate Reynolds numbers as well as relative roughness. With β calculated, the vehicle drag coefficient may be directly determined from Eq. (2-14).

III. TEST PROCEDURE/DATA ACQUISITION

A. FACILITIES

The experimental investigations were carried out in the VICS-70 and VICS-120 facilities. (VICS is an acronym for Vehicles In Confined Spaces.) Both tubes are vertically oriented with honed inner surfaces of 5.28-cm dia., which corresponds to about 1% scale. The two test section tubes are 21.3 m (70 ft) and 33.2 m (109 ft) long, respectively; vertical orientation permits the convenient use of gravity to propel the model vehicles down the test section

tubes at equilibrium as well as nonequilibrium conditions. Reynolds numbers on the order of 3×10^4 were obtained in the VICS-70 using air in an open-ended test section. In order to investigate the effects of test section tube length on model performance, constrictions in the form of orifices were used at the tube exit to effectively increase its length. Heavy gases such as CO_2 and "Freon 12" and pressurization to 1.034×10^6 N/m^2 gage increased Reynolds numbers to 10^6, with a closed test section simulating an infinitely long tunnel.

Since, under pressurization, the tube length of this earlier facility was effectively infinite, the longer, more versatile VICS-120 facility (Fig. 1) was put into operation. The ends of this test section tube are connected to a common plenum so that the tube ends are effectively open when the facility is pressurized. This was validated by making runs at atmospheric pressure with the test section first connected to the plenum and then open to atmosphere, with identical results. Reynolds numbers of up to 4×10^6 were achieved with the facility at nearly 50 atmospheres of CO_2 and model velocities of 10 m/s (the Reynolds number of a full-sized train traveling at 30 m/s is about 7×10^6). Nominal test section tube L/D is 630, which scales to a 3.2-km-long tunnel. In later experiments, a plastic roughness liner was inserted inside the VICS-120 test section tube in order to study the effects of internal ribbing. This modification increased the L/D ratio to 840 due to the smaller internal diameter.

Although a "pneumatic" catapult launcher has been built for the VICS-120, experiments to date have been performed by simply releasing the model from rest. This low-kinetic-energy operation allows the use of a rather simple arrestor. It consists of large-diameter pipe, packed with a series of plastic sponge slugs, which stack up as the model is brought to rest.

B. MODELS

It was determined early in the program that gravity-propelled, low-Reynolds-number studies required light-weight models for steady-state equilibrium investigations. Styrofoam was used in these cases, since it afforded light weight while retaining structural integrity. Lead-ballasted aluminum tube models were used for the moderate- to high-Reynolds-number tests. In order to investigate "train-like roughness," car separation grooves

and simulated window and door grooves were cut in thick-walled (0.64 cm) styrene tube models. The basic nose and tail shapes used throughout the program were hemispherical. Only a brief investigation was performed on the effects of changes in the nose and tail shapes from flat to streamlined. Highly detailed trains were simulated by using both HO- and N-gage plastic hobby-model train cars. An example of each type of model is shown in Fig. 2. All models had at least two sets of three runners or skids in order to keep them centered in the test section, since data repeatability was found to suffer without them. Brief eccentricity studies were performed and found to have little effect. The drag increased about 5% as the model approached the tube wall.

C. MEASUREMENTS

Photo-cell and side-wall static pressure transducers could be located at up to 18 positions along the VICS-120 test section tube. Since most of the program involved steady-state operation, the use of six photo-cell stations and six pressure transducer stations was found to be adequate. Model position history could then be determined from all 12 stations, yielding a rather detailed velocity history. For steady-state operation, a drag coefficient could easily be determined from the equilibrium velocity. The six pressure transducers were connected to an oscillograph and produced a detailed "signature" as the model passed, as well as discrete levels of the pressure gradient along the test section tube. This gradient was then related to the flow velocity in the tube from well known pipe friction laws. A more direct flow velocity measurement was occasionally made using a pitot-static tube near the test section exit on a few runs. In all cases, the agreement with the indirect pressure gradient method was excellent.

D. DATA REDUCTION

Determination of the model velocity along the test section was straightforward, following directly from the oscillograph record of model position history. Equilibrium or steady-state conditions were obtained in the majority of the runs. The criterion was that the model acceleration be less than 0.01 g over the last 10 m of the test section tube, where the sidewall pressure transducers were concentrated. Once a steady-state model velocity was determined, the drag coefficient C_D was easily computed by noting that,

under equilibrium conditions, the model drag is equal to its weight: C_D = drag/qa, where $q = 1/2\rho v^2$.

The flow velocity in the test section, both ahead of and behind the model, was, for the most part, inferred by the pressure gradient along the tube monitored by the side-wall pressure transducers. The well known Darcy-Weisbach pipe friction loss equation may be written:

$$\frac{\Delta P}{L} = \frac{f}{D}\frac{1}{2}\rho v^2$$

or, in terms of the ratio of the flow velocity to the model velocity,

$$\beta = \frac{V}{v} = \left(\frac{\Delta PD/Lf}{q}\right)^{1/2}$$

This is an iterative solution, however, since f is a function of the Reynolds number and hence, of q (the convergence is rapid, requiring no more than three iterations).

Friction factors on the model wall and tube wall in the annular region were determined from portions of the pressure signature as the model passed a transducer.

For nonequilibrium runs, the model drag does not equal its weight, and a more complex reduction is necessary. The "slug theory" (Section VIA) was used for $a/g > 0$ in order to calculate the ratio of the flow velocity to the model velocity β at a position near the tube exit (0.9 L) and β_{ss}, the steady-state ratio for which $\Delta\beta = 0$. The assumption is made that the normalized drag coefficient,

$$C_{D_\infty} = \frac{C_D}{(1 - \beta)^2}$$

is not sensitive to β. For model accelerations less than 0.1 g, a simplifying assumption may be made for the instantaneous drag coefficient,

$$C_{D_i} = \frac{m(g - a)}{q}$$

Therefore,

$$C_{D_{ss}} = C_{D_i}\left(\frac{1 - \beta_{ss}}{1 - \beta}\right)^2$$

Determination of the friction factors and momentum coefficients (Sections IVC and D) was not adversely affected by model accelerations of less than 0.1 g.

A more complete treatment of the data reduction procedure may be found in Ref. 3.

IV. DATA PRESENTATION

A. DRAG

The drag coefficient data for all of the conditions investigated had essentially the characteristic shown in Fig. 3 when plotted against model Reynolds number. The drag coefficient decreased with increasing Reynolds number; above a Reynolds number of about 10^6, the decrease in the drag data became quite small as Reynolds number continued to increase. This behavior with Reynolds number is much the same as the turbulent pipe flow friction factor with a distributed roughness on the pipe wall somewhere between 10^{-4} to 10^{-3} of the pipe diameter. This is true even for the ribbed-tube case. Theoretical calculations of the drag compare quite favorably with the experimental data, generally within 5%, as shown by the dotted fairings.

The effect of blockage ratio upon the drag is shown in Fig. 4. In the case of the smooth-wall tube with L/D = 630, the increase in drag coefficient with increasing blockage ratio is moderate compared to the situation for the infinite tube length or the ribbed* tube of L/D = 840. As can be seen, the effect of the ribbing (direct measurements in the VICS-120 facility yielded a pipe flow friction factor of 0.095, about six times greater than for the smooth tube) tends to give the C_D vs σ curve for the L/D = 840 ribbed tube the same characteristic as the L/D = ∞ smooth tube.

*The helical ribs, which are 0.02 D in height, are spaced on 0.22-D centers. Their cross-section is trapezoidal, with a base thickness the same as the height. See sketch in Fig. 4.

When the blockage ratios of the smooth and train-like models in the ribbed tube are based upon the diameter inside the ribs, they are 0.49 and 0.71, respectively, rather than the plotted values of 0.46 and 0.66, which are based upon the tube diameter at the base of the ribs. If the higher values of the blockage ratio are used when plotting the model drag for the ribbed tube case, the $L/D = \infty$ curve nearly coincides with the $L/D = \infty$ curve for the smooth-tube case. This suggests that the addition of ribs in a tube essentially increases the effective blockage ratio and the effective tube length for $L/D < \infty$. Therefore, a detailed knowledge of the flow in the annular region may not be required in order to estimate the effect of this type of ribbing (which yields a pipe flow friction factor about the same as many realistic subway tunnel rib geometries) on vehicle drag.

The train-like roughness approximated by annular grooves on the models generally increased the drag by about 15% for all the conditions tested. But the drag of the highly detailed HO- and N-gage models is considerably greater than that for the smooth models. This is seen in Fig. 4 for the HO-gage model in the smooth tube by comparing the + symbol with the o symbols. The increase in drag of an actual train geometry over the idealized smooth-wall cylinder is about 75%. The increase in drag for the N-gage model ($\sigma = 0.36$) in the ribbed tube is double that of the smooth cylindrical configuration.

The effect of vehicle length upon the drag coefficient increases as the blockage ratio decreases. As can be seen in Fig. 5, the ℓ/d increase from 15 to 30 for $\sigma = 0.71$ results in about a 20% increase in C_D, while for $\sigma = 0.52$, a 25% or so increase in C_D results.

In order to demonstrate the effect of tunnel length on the drag coefficient, it is necessary to rely upon theoretical calculations, since the tests in the VICS-120 facility were performed only at $L/D = 630$ (about a 3.2-km long smooth tunnel) and at L/D = infinity.* Figure 6 shows that the effect of tunnel length becomes more pronounced as the blockage ratio increases. The eight data points shown agree quite well with the theoretical data.

*In the earlier VICS-70 facility, a range of effective L/Ds from 290 to 10^4, and of course infinity, was obtained by using various sized orifices on the lower end of the tube to restrict the flow. These tests, performed at $R_d \sim 3 \times 10^4$, indicated that the theoretical model adequately predicted the effect of tube length on vehicle drag.

Unless otherwise stated, the vehicle nose and base shape was the basic hemispherical configuration. A limited study was done to determine the effect of varying the nose and base geometry. Since the study in the VICS-120 facility included blockage ratios of only 0.71 and 0.83 at $R_d \sim 10^6$, the data taken over a wider range of blockage ratios in the VICS-70 facility at a low Reynolds number are shown in Fig. 7. These two series of tests gave consistent results. The ellipsoidal-flat configuration yielded results comparable to those obtained with the standard hemispherical-hemispherical configuration. At $\sigma = 0.90$, there does not seem to be any significant effect of nose-base geometry upon drag; but at $\sigma = 0.50$, the effect of a flat nose or a streamlined base on the ellipsoidal-flat configuration is significant, being about 15% and 25%, respectively.

Usually the model was constrained to be concentric with the tube. In order to observe the effects of off-center operation, the tri-skid guides were adjusted to put one side of the model about 0.5 mm from the tube wall. These results for the test in the VICS-70 facility are shown in Fig. 8. The effect upon drag for $\sigma = 0.74$ is insignificant, while at $\sigma = 0.50$, eccentric operation increases the drag by about 5%. Tests in the VICS-120 facility at high Reynolds numbers, which gave comparable results, showed that the effects of eccentricity remained about 5% at $\sigma = 0.23$.

B. FLOW VELOCITY IN TUBE

The flow velocity was inferred from the pressure gradient in the tube ahead of the model for every run by the use of generally accepted turbulent pipe flow friction factors as a function of Reynolds number for the tube roughness factor. This procedure was verified a number of times for the smooth tube during the test program under widely different conditions by a direct measurement of the flow velocity with a frangible pitot-tube and a static pressure port on the tube wall. In the case of the ribbed tube, friction factor vs Reynolds number data were scarce, so it was necessary to make measurements of the flow velocity directly. Centerline velocities were converted to bulk flow velocities, assuming a fully developed turbulent flow profile. The friction factor was determined from an iteration procedure and found to be constant. For the remainder of the runs in the ribbed tube, the flow velocity was inferred in the usual manner from the pressure gradient.

A sample of the tube flow velocity ratio (β) data as a function of vehicle Reynolds number is shown in Fig. 9 for σ = 0.52 and 0.72. The data scatter makes it difficult to establish any trends with Reynolds number. This large scatter in the β data is not consistent with the small scatter in the C_D data, since C_D is very sensitive to β. Therefore it appears that the scatter in the β data is strictly an instrumentation and data reduction problem, even though the differences between the direct and indirect measurements of flow velocity in the tube are small and exhibit little scatter.

As a consequence of the scatter in β, smoothed values of β vs R_d were used in order to further reduce the data for each run rather than the particular β for each run. However, this approach made only a small improvement in the subsequent data analyses (momentum loss coefficients and friction factors). The fairings appearing in Fig. 9 are from the theoretical model, and are certainly compatible with the data. It is interesting to note that the theoretical fairings are nearly horizontal, both barely increasing with Reynolds number.

RMS-type fairings (slopes based upon theoretical consideration) were put through the β vs R_d data for the various blockage ratios (and other conditions) in order to derive the effect of blockage ratio on the flow velocity in the tube. The result of this is shown in Fig. 10 for both the smooth and ribbed tubes. In spite of the large scatter in the β vs R_d data, the resulting β vs σ data form a smooth, reasonable progression, and compare favorably with the theoretical curve shown for the smooth-tube case. The theoretical fairing of the two data points for the ribbed-tube case is based upon the following assumption. The ribbed-tube length was replaced by a smooth tube six times longer (the ratio of the friction factors) in L/D. The model blockage ratio was based upon the tube area inside of the ribs. The favorable comparison between the curve and the data demonstrates that this simple approach can adequately predict the bulk flow velocity in the tube. This same approach, used to estimate the drag coefficient, works equally well.

Theoretical curves of the effect of tube length upon the flow velocity in the tube are shown in Fig. 11. The experimental data at L/D = 630 agree fairly well with the theory.

C. MOMENTUM COEFFICIENTS

1. Nose

The momentum loss coefficients were determined from the pressure signature of the model during the equilibrium portion of its travel through the tube. The pressure signature is merely the pressure history at a point on the tube as the model passes it. The pressure drop as the nose of the vehicle passes over the pressure port can be expressed by a momentum loss coefficient C_1 over the model nose. From the derivation of the theoretical model, C_1 is defined as follows:

$$C_1 = \frac{a_1}{\sigma(2 - \sigma)} \left(\frac{1 - \sigma}{1 - \beta}\right)^2 \frac{1}{1/2\rho v^2}$$

where a_1 is the drop in pressure at the model nose.

A value of unity indicates that the measured pressure drop over the model nose is identical to that calculated from one-dimensional Bernoulli principles. A value below unity indicates an experimental drop less than calculated, which is a surprising result that was generally obtained for the higher Reynolds numbers and blockage ratios. This can be explained, in part, by the use of the nondimensionalizing term, which is based upon the average bulk flow velocity rather than upon the average dynamic pressure in the gas flowing through the tube.

A summary of this coefficient as a function of model blockage ratio at $R_d = 10^6$ in a smooth tube appears in Fig. 12a. Although the scatter in the C_1 vs R_d data is large, it still is possible to get an appreciation of the variables which affect it. From the C_1 vs R_d data, a typical example being shown in Fig. 13, it appears that this coefficient is affected by tube length as well as the Reynolds number (the dashed fairing shown is for Reynolds number effect at L/D = infinity). From Fig. 12a, the vehicle blockage ratio is shown to be an important parameter for $\sigma < 0.5$. At the lower blockage ratios, there are indications that C_1 is also a function of nose geometry, with a flat nose giving a larger value than the basic hemispherical nose. This increase in C_1 results in an increase in the theoretical drag, which is consistent with the trend that was experimentally observed.

2. Base

Unlike the pressure drop over the model nose, the pressure drop over the base of the model, in general, was a very difficult quantity to measure with high confidence. Fortunately, the difficulty of quantifying it is inversely related to its effect on the vehicle drag. Hence, the large scatter in the C_2 vs R_d data shown in Fig. 14 is quite acceptable. The fairing shown in this figure is typical of that for the other blockage ratios. In spite of the problem of generating meaningful fairings, a fairly consistent pattern emerged, as can be seen in the summary plot (Fig. 12b). This coefficient was obtained from the pressure signature data using the following relation based upon the theoretical model:

$$C_2 = \sigma(2 - \sigma) \frac{a_2}{a_1} C_1$$

where a_2 is the pressure drop at the model base. A value of zero indicates no pressure drop.

3. Wake

The coefficient C_3 for the pressure recovery in the wake of the vehicle is depicted as being constant in Fig. 12c. The basic C_3 vs R_d data (Fig. 15) have considerable scatter, but RMS-type fairings through all of the data result in fairly consistent results. The calculation of C_3 from the pressure signature is

$$C_3 = \frac{1}{2} \frac{2 - \sigma}{1 - \sigma} \frac{b}{a_1} C_1$$

where b is the pressure rise in the wake. In order for the momentum balance to be preserved in the theoretical model, C_3 must equal unity. Its general value of 1.25 is not too different from unity to cause concern, since the overall aerodynamic phenomenon is likely to be considerably more complicated than the scheme assumed for the simple theoretical model.

4. Sensitivity

The sensitivity of the theoretical calculated drag to variations in the C factors is generally low. Details of a sensitivity analysis for $\sigma = 0.71$ appear in Section VD. For $\sigma = 0.23$, a percentage change in C_1 affects the drag to a somewhat greater percentage, but by $\sigma = 0.83$, the effect on drag is an order of magnitude less. The effect of variations in C_2 or C_3 on the theoretical drag is about an order of magnitude less than the percentage change in C_2 or C_3 for all blockage ratios and tube lengths investigated.

D. FRICTION FACTORS

1. Tube

The large amount of readily available turbulent pipe flow friction factor data can be used to estimate the pressure gradient in the tube upstream of the vehicle. Such data are available not only for uniformly distributed roughness but also for some internal ribbing configurations. In these experiments with the ribbed tube (ribs being trapezoidal in cross-section), the experimentally determined friction factor of 0.095 can be compared with the 0.11 value that is indicated in Ref. 4 for ribbing that is similar except that the rib cross-section is square. For the smooth tube, the generally accepted turbulent pipe flow friction factor for $\epsilon/D = 10^{-4}$ as a function of Reynolds number was found to be satisfactory.

2. Vehicle Wake Effect

Because of the presence of the model wake, there is a difference in the pressure gradient along the tube downstream of the model from that upstream of the model. This difference can be accommodated by using a ratio of the downstream to upstream turbulent pipe flow friction factors. In the shorter tube (L/D = 290), the downstream friction factor was about 13% greater than the upstream one for the blockage ratios investigated ($0.5 < \sigma < 0.9$). In the longer tube facility (L/D = 630), the ratio f_D/f_U was considerably less, being unity for $\sigma = 0.23$ and increasing up to about 1.05 for $\sigma = 0.83$. The overall scatter of the data upon which these ratios are based is shown by the vertical scatter bars in Fig. 16; it is felt that the indicated fairings (which are based on all the data) are quite indicative of the actual situation. It is reasonable that the ratio of f_D/f_U decreases

toward unity as the tube length increases, since the measured pressure gradients are an average value for the entire distance from the tube entrance to the model just before it exited the tube.

3. Annular Region

The annular friction factor for the smooth tube wall case is shown in Fig. 17 for $\sigma = 0.52$ and 0.71. As a guide for determining a representative fairing through the data, the Nikuradse curve for $\epsilon/D = 10^{-3}$ and a level curve for $\epsilon/D = 10^{-4}$ are included along with the smooth-wall curve for the turbulent pipe flow friction factor as a function of Reynolds number. The annular Reynolds number is based on the flow velocity in the annular region relative to the vehicle and on the annular diameter (D - d). In calculating these friction factors from the annular gradient portion of the pressure signature, the simplifying assumption was made that the friction factors on the model and tube wall in the annular region were the same. This is not quite true because of the difference in Reynolds number on the tube wall from that on the model wall. However, based upon the theoretical model and the generally accepted smooth-wall circular pipe friction curve, they are within 5% of each other.

The effective roughness parameter (ϵ/D) in the annular region for the smooth model in the smooth tube is between 10^{-3} and 10^{-4}. The annular friction factors are in the general vicinity of the circular pipe ones. As can be seen by comparing Fig. 17a with Fig. 17b, the annular friction factor decreases somewhat with increasing blockage ratio. A summary of the annular friction factor as a function of vehicle blockage ratio is shown in Fig. 18 for an annular Reynolds number of 5×10^5 (which more or less corresponds to $R_d = 10^6$). It clearly shows the trend of a decreasing friction factor with increasing blockage ratio. The dashed horizontal fairings are the usual circular tube data.

Also included in Fig. 18 are the results for the ribbed-tube case, which have the same characteristics but at a 30% higher level. Except for the higher level, the data of the annular friction factor as a function of annular Reynolds number for the ribbed-tube case (see Fig. 19) look just like the data for the smooth tube shown in Fig. 17. In reducing the annular friction factor data, an effective blockage ratio was used, based upon the tube area inside the ribs, giving $\sigma = 0.49$ and 0.71 rather than $\sigma = 0.45$ and 0.66,

respectively. Here again, the assumption was made that the friction factor in the annular region was the same on both the tube wall and model wall. Since this is not a valid assumption because of the considerable difference in wall roughnesses, the annular friction factors shown are the effective values, and can be used only for cases where the relative roughnesses are the same as those used for these studies. In the long run, this is no real problem, because the data can be re-reduced once one assumes a ratio for the tube-to-model wall friction factors. This is done by an iterative process, using the smooth-wall data to establish the initial ratio for the next calculation step. The first iteration would assume that the tube wall annular friction factor is 1.3 times that for the smooth model (because of the 30% higher effective factor shown in Fig. 18).

One step in the data reduction for the annular friction factor should be pointed out. The annular gradient in the pressure signature must be reduced by the gradient along the tube ahead of the model. This is necessary in order to convert the data from a point in space to a point in time (which is the basis for the theoretical model).

V. ANALYSIS

A. ELEMENTS OF AERODYNAMIC DRAG

The simplified theoretical model presented earlier shows the total aerodynamic drag to be composed of the following five basic elements:

(1) Bernoulli effects at the vehicle nose (referred to as form drag for brevity).

(2) Friction force on the cylindrical wall of the vehicle.

(3) Pressure gradient in the annular region due to skin friction on the cylindrical wall of the vehicle.

(4) Pressure gradient in the annular region due to skin friction on the tube wall immediately surrounding the vehicle.

(5) Pressure drop as the flow expands over the vehicle base (referred to as base drag for brevity).

Since the theoretical model, using the experimentally determined coefficients (C and f) adequately predicts both the aerodynamic drag and the

tube flow velocity over a wide range of conditions, it is reasonable to expect that the use of this theoretical model will do a realistic job of separating the total aerodynamic drag into its basic elements.

Should one desire to evaluate the contribution of the various elements to the total drag, the use of the theoretical model is a real convenience because doing so by direct measurements would be extremely difficult. Figure 20 shows the relative contribution of these five elements* to the total aerodynamic drag for the basic test condition.

The dominant contribution of the drag is from the Bernoulli pressure drop effect over the nose; for an L/D = 630 smooth-wall tube, it contributed about 65% of the drag at $\sigma = 0.23$, about 40% at $\sigma = 0.23$, and about 40% at $\sigma = 0.83$. The contribution of the sum of the two elements of the vehicle wall skin friction varies from 28 to 40% as the blockage ratio increases. The expansion over the base makes a very moderate contribution, going from about 7 to 12%. At the lowest blockage ratio tested, the effect of the tube wall friction in the annular region is negligible, and increases up to only 6% for $\sigma = 0.83$.

The effect of either longer tubes or tubes with internal ribbing is mainly to increase the contribution of the annular pressure gradient due to the tube wall skin friction in the annular region at the expense of all the other elements. This increase can be significant, becoming about as much as one-fourth of the overall drag at the highest blockage ratio.

B. PRESSURE SIGNATURE CHARACTERISTICS

The major effect upon the characteristics of the pressure signature is due to the blockage ratio. Typical pressure signatures are shown in Fig. 21 for the four main blockage ratios examined in the VICS-120 facility. The major effects of increasing blockage ratio on the shape of the signatures is an increase in the annular pressure gradient and a decrease in the

*Even though there are five distinct elements, one must not neglect the fact that the vehicle wall friction drag and the pressure gradient in the annular region due to the friction on the vehicle wall are really not separable in the sense that one cannot exist without the other and perhaps should be considered as a single element. Nevertheless, in this report, they are taken to be separate identifiable (although directly related) elements.

pressure rise in the wake relative to the pressure drop over the model nose. In order to quantify the major characteristics, the pressure signature is divided into the five pressure steps shown in Fig. 22. The pressure signatures obtained for each run have been analyzed using the definition of the pressure characteristics described in Fig. 22, where Δ is used to normalize the other four pressure steps.

A descriptive sample of these pressure characteristics is shown in Fig. 23 to serve as a basis for comparing the characteristics of pressure signatures obtained in other investigations. Both a_1/Δ and b/Δ are strong functions of blockage ratio, while a_2/Δ and c/Δ are weak functions of the blockage ratio. These data are for the higher Reynolds number conditions ($R_d > 10^5$) in a smooth-wall tube.

C. DRAG INFERRED FROM PRESSURE SIGNATURE

The steady-state drag data presented in this report were obtained by equating the drag force to the model weight, a simple, direct way of measuring the aerodynamic drag under the equilibrium test conditions achieved during these investigations. However, it should be possible to infer the drag from the pressure signature. From theoretical considerations, assuming one-dimensional flow, the drag force is equal to the pressure drop across the vehicle (the value Δ shown in Fig. 20) times the tube cross-sectional area, decreased by the friction force on the tube in the annular region and by the pressure drop that occurs in the tube ahead of the vehicle for a distance equal to the length of the vehicle:

$$\text{Vehicle drag} = A\Delta - \frac{\pi}{4} f_T D\ell \left(\frac{\sigma - \beta}{1 - \sigma}\right)^2 \frac{1}{2}\rho v^2 - \Delta p_1 \frac{\ell}{L_U}$$

The two negative terms in the above expression are generally small: less than 5% of $A\Delta$. Neglecting them results in an approximate form of the pressure-inferred drag of

$$C_{D_p} = \frac{A\Delta}{1/2\rho v^2 a}$$

A fairly extensive sample of the relationship of this pressure drag coefficient with the model-weight drag coefficient is shown in Fig. 24. As can be seen, the comparison is quite favorable, the average being just below the line of exact correspondence.

The consequences of this favorable comparison of the pressure-signature-inferred drag with the model weight drag are far-reaching. It is a direct confirmation that aerodynamic drag can be obtained by an extremely simple technique – accurate pressure measurements. This means that very simple test setups can be used to obtain the aerodynamic drag of vehicles traveling in tubes, not only in model-scale tests but in field tests on full-scale train-subway systems. It is not necessary to rely upon the complex, and generally unsatisfactory technique of measuring the deceleration of a coasting train in order to infer the aerodynamic drag.

D. SENSITIVITY OF PREDICTED VEHICLE DRAG COEFFICIENT TO VARIATIONS IN CONSTANTS

The relative importance of the various momentum constants (C) and friction factors (f) that are used in the analytical models should be known in order to place proper emphasis on the requirements of obtaining and using them. Therefore, a limited analytical study was performed to determine the sensitivity of the calculated vehicle drag coefficient to changes in the values of the arbitrary constants used in the flow velocity ratio and drag coefficient expressions in the theoretical model described in Section II.

This analytical sensitivity study was carried out for one blockage ratio under two conditions: (1) a vehicle traveling in a smooth-wall tube with an effective length-to-diameter ratio (L/D) of infinity (obtained by closing off the lower end of the test section tube); and (2) a tube with an L/D of 630. These two cases approximate the conditions for many of the experimental runs which were made in the VICS-120 facility.

In order to determine the sensitivity of C_D to the annular friction factor and the various momentum coefficients, the nominal values shown in Table 2 were first assumed. Each of the coefficients was, in turn, increased and decreased by 20%, and the change in the drag coefficient (C_D) was determined.

Table 3 summarizes the result for this blockage ratio. Since a positive variation in the constants had essentially the same proportional effect upon the drag coefficient as a negative variation, only the averages of the effects on C_D for the positive and negative variations of the constants are shown. In every case, an increase in any of the constants resulted in an increase in C_D.

For the L/D = infinity case, the effect of variations in the C constants decreases with increasing vehicle blockage. The constant C_1 is the dominant one in predicting drag coefficient. The sensitivity to friction factor is less at the lower blockage ratios; at the higher blockages, the friction factor becomes significant and dominates the sensitivity of the C factors.

For the L/D = 630 case, the same qualitative trend with blockage ratio on C_D is still true for C_1, but to a lesser degree. However, the effect of annular friction factor decreases with increasing vehicle blockage ratio, rather than the reverse noted for the L/D = infinity case. This is because the tube flow velocity ratio increases with increasing blockage ratio, hence minimizing friction effects compared to the L/D = infinity case, where the tube flow velocity remains zero.

The use of the nominal values of the momentum coefficients and the friction factors for predicting vehicle drag by means of the theoretical model is verified by the generally good agreement between the experimental data and the calculated values.

VI. UNSTEADY AERODYNAMICS

An actual subway train may spend very little time operating under steady-state conditions. In order to perform design studies, it is, therefore, necessary to understand the aerodynamic consequence of unsteady operation. A simple theory is presented and a sample problem is discussed in order to give the reader an appreciation of the importance of aerodynamics in the system.

A. SLUG THEORY

When a model is accelerating (or decelerating) throughout the test section, the drag is never equal to its weight, and the data reduction becomes more complex. As shown in Sketch 4, the far-field drag is made up of four distinct parts:

(1) Pressure difference across the ends of the tube.

(2) Wall friction up- and downstream of the model.

(3) Wall friction in the annular region.

(4) Flow acceleration forces.

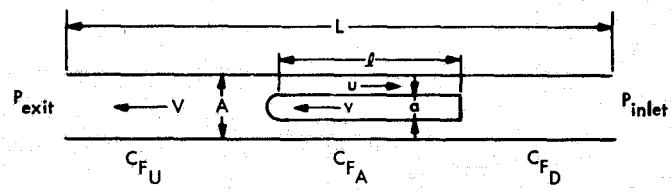

Sketch 4

Assuming that the flow is incompressible (a generally good approximation for low acceleration rates as per Ref. 5), the far-field drag may be written as follows:

$$D_{FF} = (P_{exit} - P_{inlet})A + \frac{1}{2}\rho V^2 \pi D(L - \ell)C_F - \frac{1}{2}\rho u^2 \pi D \ell C_{F_A} + \rho A (L - \ell)\frac{dV}{dt} \tag{6-1}$$

where, for the sake of simplicity, $C_{F_U} = C_{F_D} = C_F$, the effective skin friction coefficient on the pipe wall.

The near-field drag may be more familiarly written:

$$D_{NF} = \frac{1}{2}\rho v^2 C_D a \tag{6-2}$$

but here we will introduce and substitute a term called the normalized drag coefficient, .

$$C_{D_\infty} = \frac{C_D}{(1 - \beta)^2} \tag{6-3}$$

which is relatively insensitive to β (Ref. 3), so that

$$D_{NF} = \frac{1}{2}\rho v^2 a C_{D_\infty} (1 - \beta)^2 \tag{6-4}$$

Using the following relationships,

$$\sigma = \frac{P_{inlet} - P_{exit}}{1/2\rho V^2}$$

$$f = 4C_F$$

$$V = \beta v$$

$$a = \sigma A$$

$$u = v\,\frac{\sigma - \beta}{1 - \sigma}$$

$$D_{FF} = D_{N_F}$$

where both β and v are functions of time, and everything else is assumed constant (independent of time and/or Reynolds number), and defining

$$F = f\frac{(L - \ell)}{D} - \alpha$$

$$\bar{\rho} = \frac{1}{2}\rho A$$

$$\bar{L} = (L - \ell)$$

$$\bar{f}_A = \frac{1}{4}\frac{\pi D \ell f_A}{A} = \frac{\pi D \ell C_{F_A}}{A}$$

then

$$F\bar{\rho}v^2\beta^2 + 2\bar{\rho}\bar{L}\left(\beta\frac{dv}{dt} + v\frac{d\beta}{dt}\right) - \bar{\rho}\bar{f}_A v^2\left(\frac{\sigma - \beta}{1 - \sigma}\right)^2 = \bar{\rho}\sigma v^2 (1 - \beta)^2 C_{D_\infty} \tag{6-5}$$

For the usual case, where $v = v(t)$ is known and $\beta(t)$ is to be determined, Eq. (6-5) may be rewritten as

$$\frac{d\beta}{dt} = \frac{\sigma}{2\bar{L}}\left[C_{D_\infty} + \bar{f}_A\frac{\sigma}{(1-\sigma)^2}\right] - \frac{1}{2\bar{L}}\left[F - \sigma C_{D_\infty} - \frac{\bar{f}_A}{(1-\sigma)^2}\right]v\beta^2 - \frac{\sigma}{\bar{L}}\left[C_{D_\infty} + \frac{\bar{f}_A}{(1-\sigma)^2}\right]v\beta - \frac{\beta}{v}\frac{dv}{dt} \tag{6-6}$$

or

$$\frac{d\beta}{dt} = v(C_1 - C_2\beta - C_3\beta^2) - \frac{\beta}{v}\frac{dv}{dt} \tag{6-7}$$

where

$$C_1 = \frac{\sigma}{2(L - \ell)} \left[C_{D_\infty} + \frac{\pi D \ell}{4A} \frac{\sigma}{(1 - \sigma)^2} f_A \right]$$

$$C_2 = \frac{\sigma}{(L - \ell)} \left[C_{D_\infty} + \frac{\pi D \ell}{4A(1 - \sigma)^2} f_A \right]$$

$$C_3 = \frac{1}{2(L - \ell)} \left[f \frac{L - \ell}{D} - \alpha - \sigma C_{D_\infty} - \frac{\pi D \ell}{4A(1 - \sigma)^2} f_A \right]$$

With the velocity history known, the unsteady drag of the vehicle may be computed by first solving for $\beta(t)$ from Eq. (6-7) and using that result in Eq. (6-4). Note that the equilibrium flow velocity ratio β may be determined from Eq. (6-7) by setting both $d\beta/dt$ and dv/dt equal to zero.

B. SYSTEM POWER REQUIREMENTS

The time that an intra-urban subway train operates under steady-state conditions may be only a small portion of its total running time. Even though the train might reach its cruise speed in the order of a minute, the tunnel flow velocity upstream or downstream may not stabilize for several minutes (if at all), depending upon the length of the tunnel (Ref. 6). The forces on a train which must be overcome by the propulsion units may be broken into three categories: aerodynamic, inertial, and frictional.

The aerodynamic forces are a function of the velocity squared, and the horsepower requirement is a function of the velocity cubed. Figure 25 presents the cruise horsepower required as a function of velocity for a three-car train. The rolling friction between steel wheel and rail is also shown in this figure for the same twelve-axle train. Under unsteady conditions, however, the flow in the tunnel, as well as the train, is accelerating. Therefore, additional forces are involved.

In order to best show the interrelationships between the power available and unsteady power requirements, a sample case will be described.

Passenger comfort requirements dictate that train accelerations do not exceed 0.1 g or about 1 m/s^2. The example, then, will consist of a 82,000-kg, three-car, 62% blockage-ratio train (with realistic detailing and undercarriage) with a total of 1120 kW of power at the rail, accelerating from rest at a vented-to-atmosphere station through a 3.2-km unvented tunnel. Cases are presented for both a smooth-walled tunnel and one with a typical internal ribbing configuration. The train increases its acceleration slowly when moving out of the station until it reaches an acceleration of 1 m/s^2 and holds that as long as possible with the power available. That is, this is a constant power operation with a constraint of 1 m/s^2 as the maximum acceleration. Figure 26a presents the resulting velocity schedules in the two tunnels. It becomes readily apparent that the train is power-limited in both cases, with accelerations falling to less than 1 m/s^2 after less than 20 s, when it has reached a speed of 13 m/s. The train operating in the ribbed tunnel reaches its maximum cruise velocity of only 22 m/s after about 80 s. The train in the smooth tunnel would require almost 2-1/2 min to reach its cruise velocity of just under 31 m/s. If there is another station stop at the end of the 3.2-km tunnel and if the train were able to decelerate at 1 m/s^2 (this may not be practical because of the braking requirements from cruise velocity and the inertia of the air flow in the tunnel as the train approaches a stop), the train in the smooth tunnel would have to start decelerating after only about 110 s and would therefore never reach maximum cruise conditions. Using this schedule, then, the 3.2-km station-to-station journey would take about 3 min in the ribbed tunnel, and just over 2-1/2 min in the smooth tunnel.

The air flow rate in the two tunnels during this operation is shown in Fig. 26b. Notice that the flow accelerates much more rapidly in the ribbed tunnel, even though it will equilibrate at a much lower velocity.

The instantaneous drag coefficient is shown in Fig. 26c and reflects the situation exhibited by the tunnel flow velocity. That is, during the first few seconds, the flow is essentially at rest and the tunnel appears to the train to be infinitely long; hence, the drag coefficient (not the drag force) is at its maximum. As the flow speeds up, the drag coefficient begins to decrease (more rapidly in the ribbed tunnel since the flow acceleration is higher). It should also be pointed out that for a train entering a tunnel at a

speed which it maintains throughout the tunnel, both the drag coefficient and the drag force are at their maximum when the train first enters, and both decrease to their steady-state values.

In order to gain perspective into the importance that aerodynamics plays in the system, power requirements are shown in Figs. 27 and 28. Figure 27 shows the relative importance of the three contributors that were considered in the system power requirement for the smooth tunnel case. The rolling friction is only a weak function of the velocity and accounts for only about 45 kW at 30 m/s. The power required to accelerate the train mass is clearly dominant during the initial acceleration period. As the velocity is increased to, say, 15 m/s (21 s), aerodynamic drag draws more than a fourth of the total system power available, and that increases to over 75% as 30 m/s is approached. The situation is even more dramatic in the ribbed tunnel shown in Fig. 28. Here the aerodynamic drag becomes the dominant component (drawing more than half the total power available) when the train is traveling only 16 m/s and accounts for well over 90% of the available horsepower at cruise conditions which are limited to less than 23 m/s.

VII. RECOMMENDATIONS

Because of the excellent results that have been obtained, it is possible to observe certain problem areas that were not originally anticipated. In order to apply data from tests in small-scale facilities to actual full-scale systems with a high degree of confidence, the following additional studies should be performed.

Tests on the effects of major protuberances such as wheel trucks should be carried out in order to establish the value of the protuberance coefficients in the near-field theory of Ref. 6.

An additional series of tests should be performed on models with realistic geometric details in order to help develop confidence in applying the current data to full-scale trains traveling in tunnels by use of the theoretical models. This is important because the large increase in drag measured for geometrically realistic train models as represented by the highly detailed HO- and N-gage model train cars has led to concern about

applying the small-scale facility data of idealized train models to a full-scale system. To date, only a half-dozen runs using HO- and N-gage train models) have been made with such detailed configurations.

The experimental program in the rib-roughness tube of the VICS-120 facility should be extended. Only two blockage ratios were investigated (45 and 66%) at a single tunnel-rib geometry. Data at a lower and a higher blockage ratio, longer train lengths, and a variation in the rib geometry are required in order to firmly establish the basis for applying tunnel roughness scale data to equivalent full-scale systems.

VIII. SUMMARY

The main purposes of these studies were to obtain information necessary for the development of a near-field theoretical model and to provide verification of the aerodynamic scaling laws involved in high-blockage subway systems. Both of these purposes were achieved. The results point out that high-blockage subway systems have major aerodynamic considerations peculiar to this type of application. The aerodynamic forces may be one to two orders of magnitude greater than outside the tunnel. When an intra-urban train is traveling at cruise conditions, the aerodynamic forces can dominate the power requirements. When the train is operating under unsteady conditions, such as accelerating out of a station, the inertial forces are expected to be a dominant part of the power requirements only during the initial stages, even though the aerodynamic drag coefficient may be at its maximum. However, as shown in the examples presented in this paper, the aerodynamic forces are extremely important under steady cruise conditions and limit the unsteady operation in terms of maximum power acceleration. It is obvious, then, that aerodynamics should be made an essential part of the system design tradeoff study.

The aerodynamic data obtained in this experimental investigation, only a small portion of which is included in this report, cover a very extensive range of conditions that are thought to be applicable to actual subway-train rapid transit systems. When these aerodynamic data are used in detailed system analysis, it will be possible to determine whether they cover a sufficient range of conditions to an adequate degree of precision.

DEFINITION OF SYMBOLS

a cross-sectional area of vehicle

A cross-sectional area of tube

A_r cross-sectional area of tube inside ribs

C_D aerodynamic drag coefficient $= \dfrac{\tilde{D}}{1/2\rho v^2 a}$

C_{D_P} aerodynamic drag coefficient $= \dfrac{(P_u - P_d)A}{1/2\rho v^2 a}$

C'_{D_P} aerodynamic drag coefficient

$$= \frac{(P_u - P_d) - (\Delta P/\Delta L)_{\text{upstream}} \ell A - F_w}{1/2\rho v^2 a}$$

d diameter of vehicle

D inside diameter of smooth tube

$\tilde{D}$ aerodynamic drag

D_r diameter of tube inside ribbing

f friction factor on test section tube wall

f_A annular friction factor for $\gamma_f = 1$

f_T friction factor on tube wall in vicinity of model

f_V friction factor on model wall

F force

F_w drag force on tunnel wall surrounding model $= \frac{1}{2}\rho\left[v\frac{\sigma - \beta}{1 - \sigma}\right]^2 \pi D \ell \frac{f_T}{4}$

g acceleration of gravity

h tunnel rib height

ℓ length of vehicle

L length of tunnel

m	mass
P	static pressure
P_U	static pressure immediately upstream of vehicle
P_D	static pressure immediately downstream of vehicle
ΔP	pressure difference
R_d	Reynolds number = $\frac{\rho v d}{\mu}$
R_D	tunnel flow Reynolds number = $\frac{\rho V D}{\mu}$
$R_{(D-d)(u+v)}$	Reynolds number = $\frac{\rho (u + v) (D - d)}{\mu}$
u	velocity of flow relative to test section in annular region
V	air velocity relative to test section
v	vehicle velocity relative to test section
$\dot{v}$	train acceleration
β	bulk flow velocity ratio = V/v
γ	ratio of specific heats = C_p/C_v
γ_f	constant of proportionality = f_T/f_V
γ_ϵ	spacing of roughness
σ	blockage ratio = a/A
σ_r	rib blockage ratio = a/A_r
ϵ	roughness height
ν	kinematic viscosity = μ/ρ
μ	viscosity
ρ	density

REFERENCES

1. Daugherty, R.L., "Piston Effect of Trains in Tunnels," Transactions of the ASME, February 1942.

2. Subway Environmental Design Handbook, Vols. I and II, Associated Engineers, Transit Development Corp., Washington, D.C., 1974.

3. Data Acquisition for Vehicles in Confined Spaces (VICS-70) Facility, Interim Report, IRT TR UMTA-DC-MTD-7-71-8, California Institute of Technology, Pasadena, Calif., June 1971.

4. Webb, R.L., "Turbulent Heat Transfer in Tubes having Two-Dimensional Roughness, Including the Effect of Prandtl Number," University of Minnesota, Ph.D. Thesis, Mechanical Engineering, 1969.

5. Preliminary Wave Analysis of Unsteady Subway Vehicle Aerodynamics, Institute for Rapid Transit TR No. UMTA-DC-MTD-7-71-33, C California Institute of Technology, Pasadena, Calif., October 1971.

6. Kurtz, Donald W., and Dayman, Bain Jr., "The Importance of Aerodynamics in the Design of Intra-Urban Trans Traveling in Tunnels," High Speed Ground Transportation Journal, Vol. 7, No. 3, Fall 1973.

BIBLIOGRAPHY

Dayman, Bain, Jr., and Kurtz, Donald W., "Experimental Studies Relating to the Aerodynamics of Trains Traveling in Tunnels at Low Speeds," BHRA Paper G2, presented at the International Symposium on the Aerodynamics and Ventilation of Vehicle Tunnels, University of Kent, Canterbury, England, April 1973.

Harris, G.L., Theoretical Aerodynamic Near Field of Subway Train in Tunnel," GALCIT Report, California Institute of Technology, Pasadena, Calif., July 1972.

Kurtz, Donald W., "Aerodynamics of Vehicles in Tubes," Jet Propulsion Laboratory Quarterly Technical Review, Vol. I, No. 2, Jet Propulsion Laboratory, Pasadena, Calif., July 1971.

Kurtz, Donald W., and Dayman, Bain Jr., "Experimental Aerodynamic Studies for Intra-Urban Trains Traveling in Tunnels," AIAA Paper No. 73-155, presented at the 11th AIAA Aerospace Sciences Meeting, Washington, D.C., January 1973.

Marte, Jack E., "The Design and Operation of a Large Tube-Vehicle Aerodynamic Testing Facility, "AIAA Paper No. 72-1001, Palo Alto, Calif., September 1972.

Experimental Aerodynamic Characteristics of Vehicles in Confined Spaces, Institute for Rapid Transit TR No. UMTA-DC-MTD-7-72-13, California Institute of Technology, Pasadena, California, December 1972.

Table 1. VICS run summary

Blockage ratio σ	Model length ℓ/d	Nose	Tail	Model wall roughness	Reynolds Number R_d	Test section length L/D	Test section roughness
0.23	15, 30	Hemi.	Hemi.	Smooth	5×10^5 - 3×10^6	630, ∞	Smooth
0.36	14	Flat	Flat	Detailed[a]	$2.4 - 3.6 \times 10^5$	845, ∞	Ribbed
0.45	15	Hemi.	Hemi.	Smooth and train-like	2×10^5 - 10^6	845, ∞	Ribbed
0.50	15	Ellipsoidal	Flat	Smooth	3×10^4 - 2×10^5	∞	Smooth
0.52	15, 30	Hemi.	Hemi.	Smooth and train-like	2×10^5 - 9×10^5	630, ∞	Smooth
0.62	14	Flat	Flat	Detailed[b]	3×10^5	630	Smooth
0.66	15	Hemi.	Hemi.	Smooth and train-like	6×10^4 - 10^6	845, ∞	Ribbed
0.71	15, 30	Hemi., flat, Ellipsoidal	Hemi., flat, 3-dia. ogive	Smooth and train-like	3×10^4 - 3×10^6	630, ∞	Smooth
0.74	15	Ellipsoidal	Flat	Smooth	2×10^4 - 8×10^4	∞	Smooth
0.83	15, 30	Hemi., flat	Hemi., flat, 3-dia. ogive	Smooth	3×10^5 - 4×10^6	630, ∞	Smooth
0.90	15	Ellipsoidal	Flat	Smooth	4×10^3 - 2×10^4	∞	Smooth

[a] N-gage scale train model.

[b] HO-gage scale train model.

Table 2. Nominal momentum coefficient values

σ	L/D	C_1	C_2	C_3	f_A
0.71	630	1.00	0.16	1.25	0.012
0.71	∞	0.85	0.16	1.25	0.012

Table 3. Percent variation in C_D for a 20% variation in the C constants (all walls smooth, $\sigma = 0.71$, $\ell/d = 15$, $R_d = 10^6$)

Constant	ΔC_D, %	
	L/D = 630	L/D = ∞
C_1	8	15
C_2	0	1
C_3	4	-[a]
f_A	4	11

[a] C_3 does not enter C_D calculation for L/D = ∞.

Fig. 1. VICS-120 facility under construction

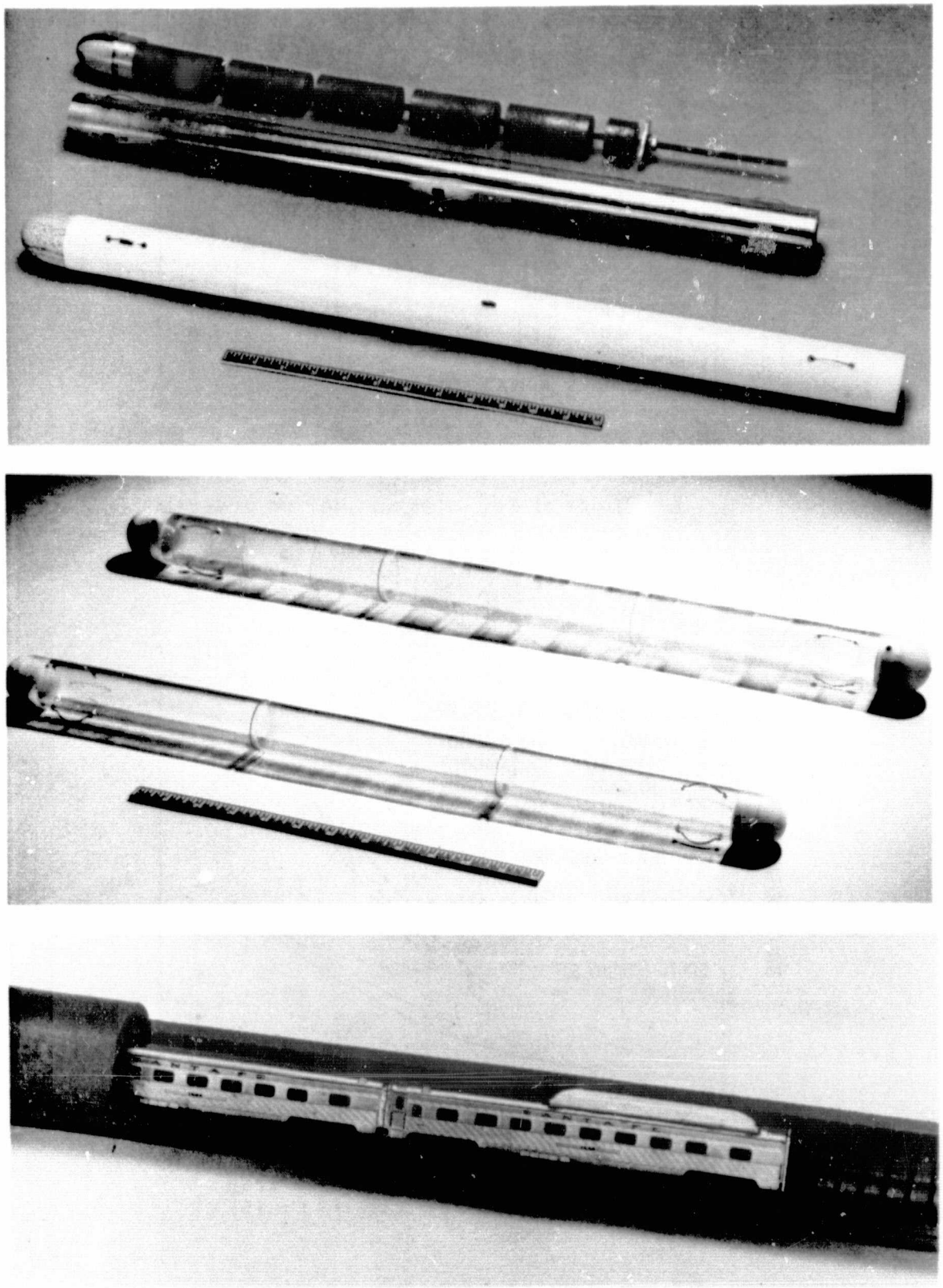

Fig. 2. Models of vehicles tested

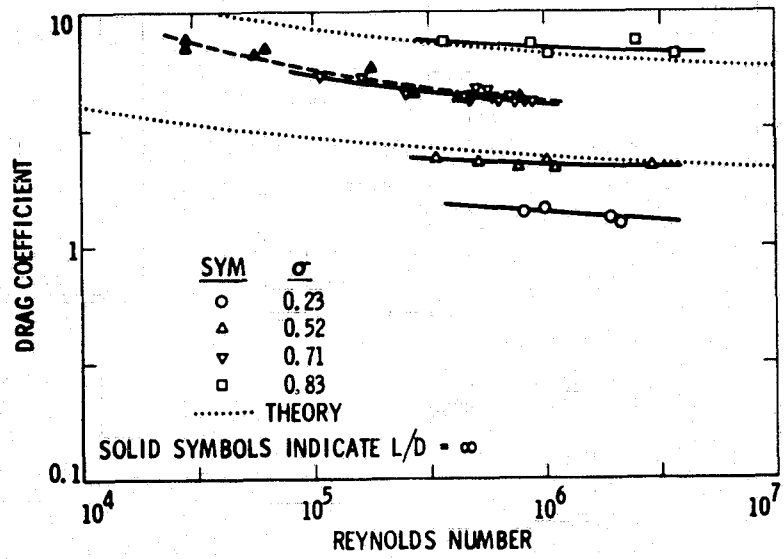

Fig. 3. Effect of Reynolds number on drag coefficient (all walls smooth, L/D = 630, ℓ/d = 15)

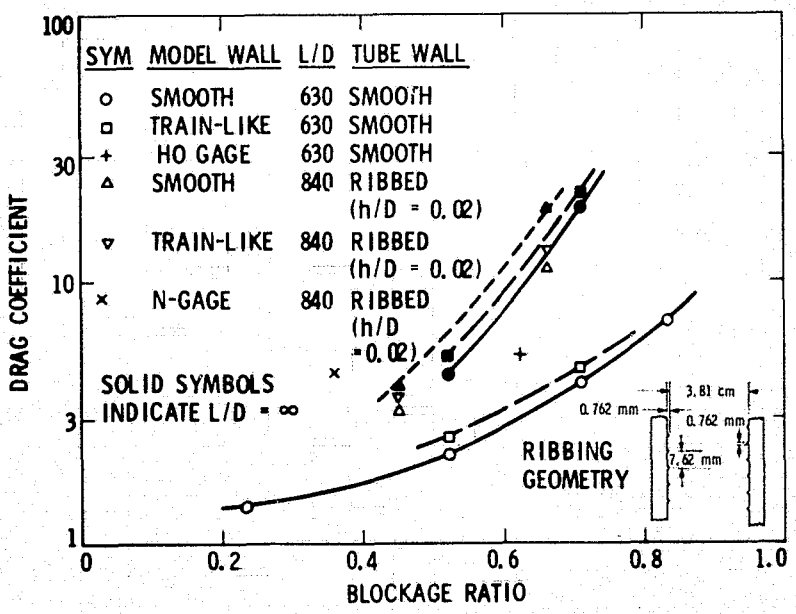

Fig. 4. Effect of blockage ratio on drag coefficient ($R_d = 10^6$, ℓ/d = 15)

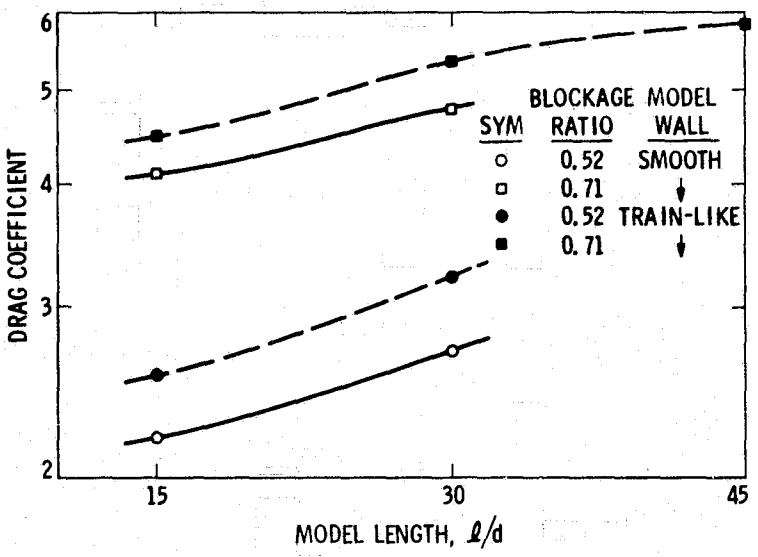

Fig. 5. Effect of vehicle length on drag coefficient ($R_d = 10^6$, smooth tube wall, L/D = 630)

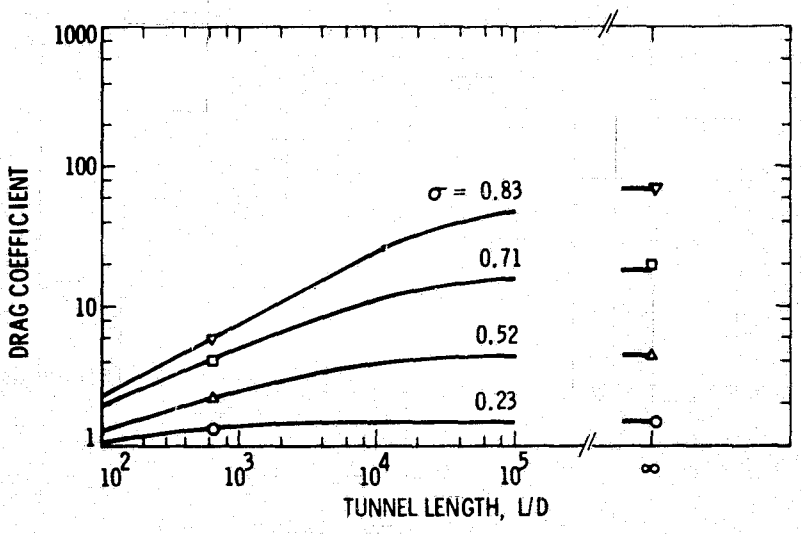

Fig. 6. Effect of tube length on drag coefficient ($R_d = 10^6$, all walls smooth, $\ell/d = 15$)

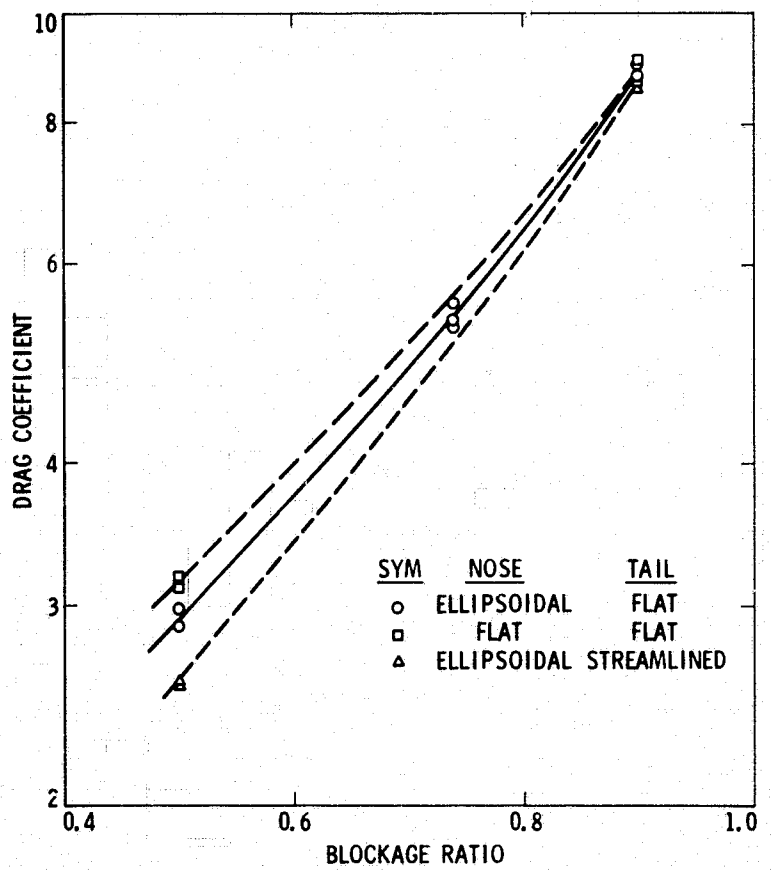

Fig. 7. Effect of vehicle nose and base shape on drag coefficient ($R_d = 3 \times 10^4$, all walls smooth, L/D = 290, $\ell/d = 15$)

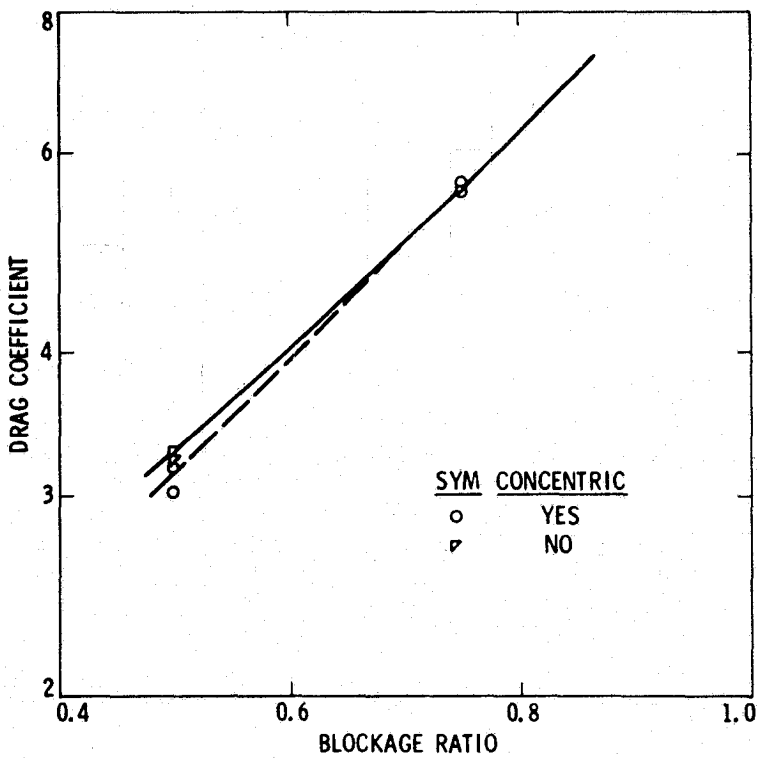

Fig. 8. Effect of eccentricity on drag coefficient (R_d = 2-1/2 × 10^4, all walls smooth, L/D = 404, ℓ/d = 15)

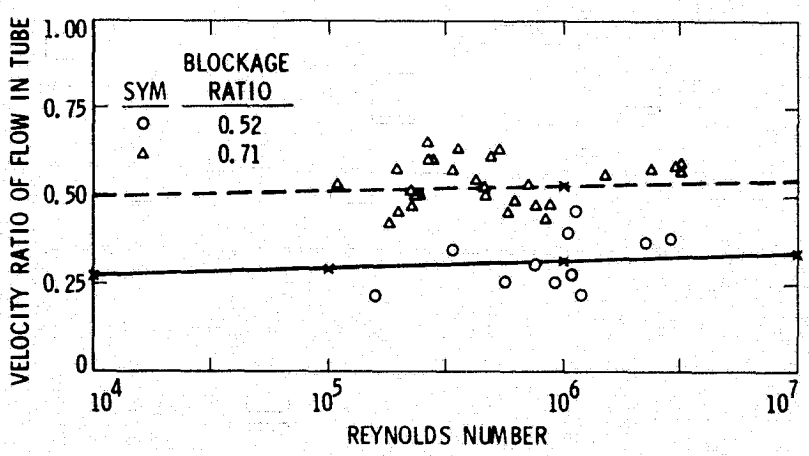

Fig. 9. Effect of Reynolds number on velocity ratio of flow in tube (all walls smooth, L/D = 630, ℓ/d = 15)

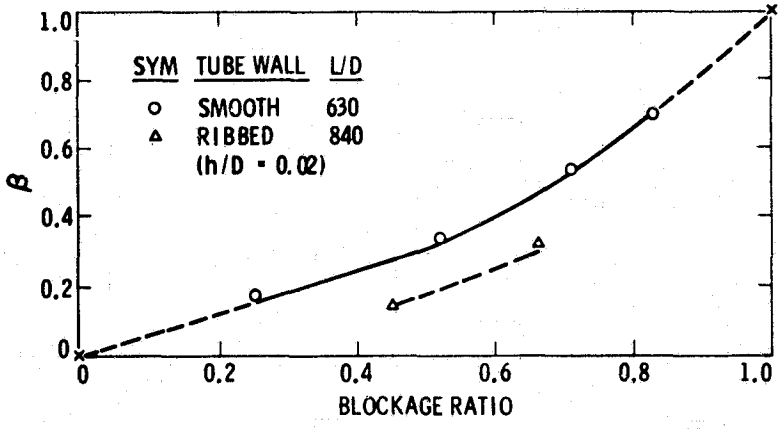

Fig. 10. Effect of vehicle blockage ratio on velocity ratio of flow in tube ($R_d = 10^6$, smooth model wall, $\ell/d = 15$)

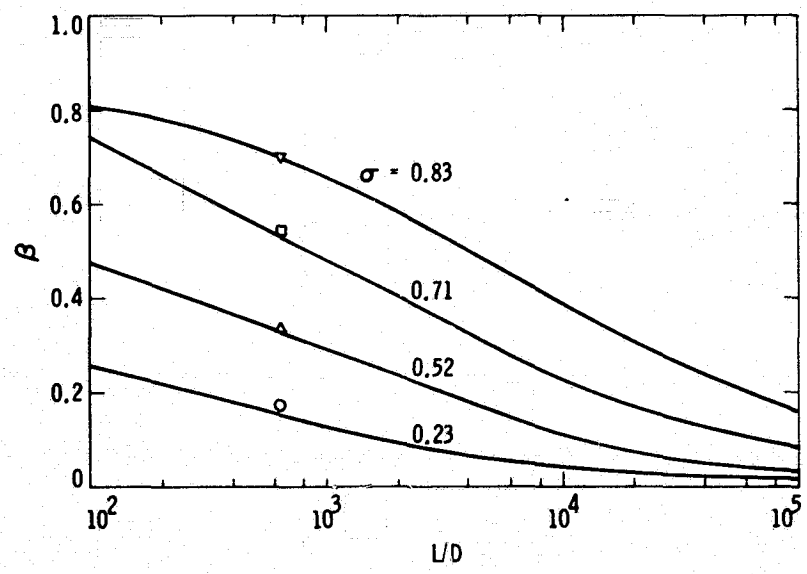

Fig. 11. Effect of tube length on velocity ratio of flow in tube ($R_d = 10^6$, all walls smooth, $\ell/d = 15$)

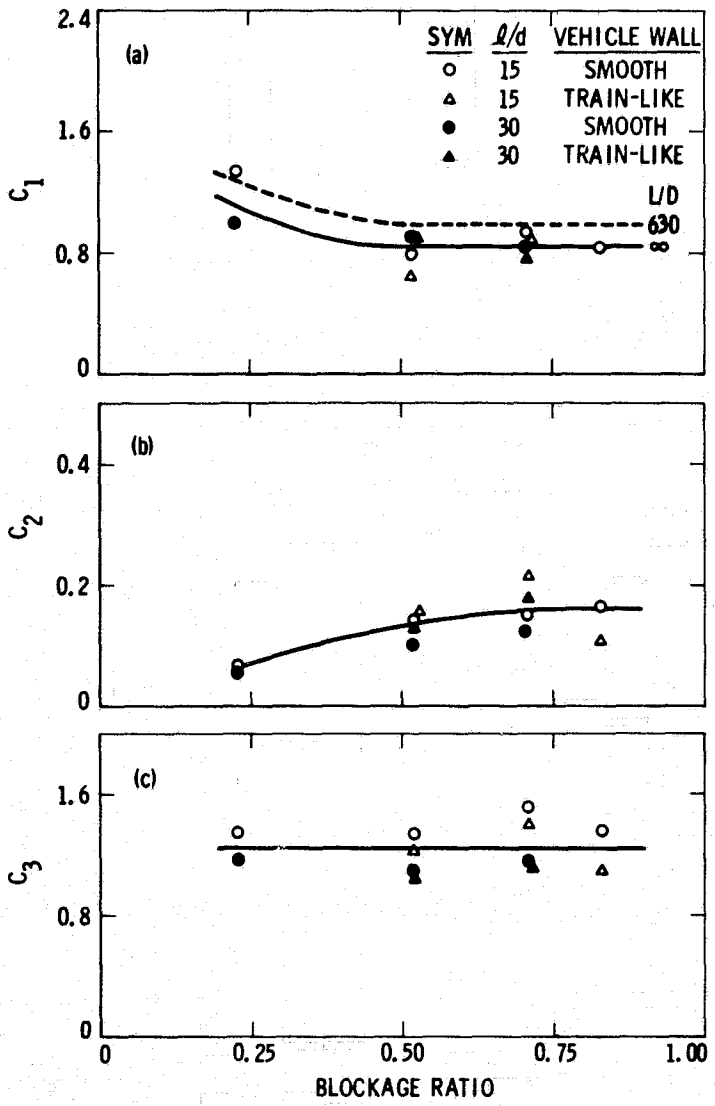

Fig. 12. Effect of vehicle blockage ratio on momentum coefficients ($R_d = 10^6$, smooth tube wall, L/D = 630 and ∞)

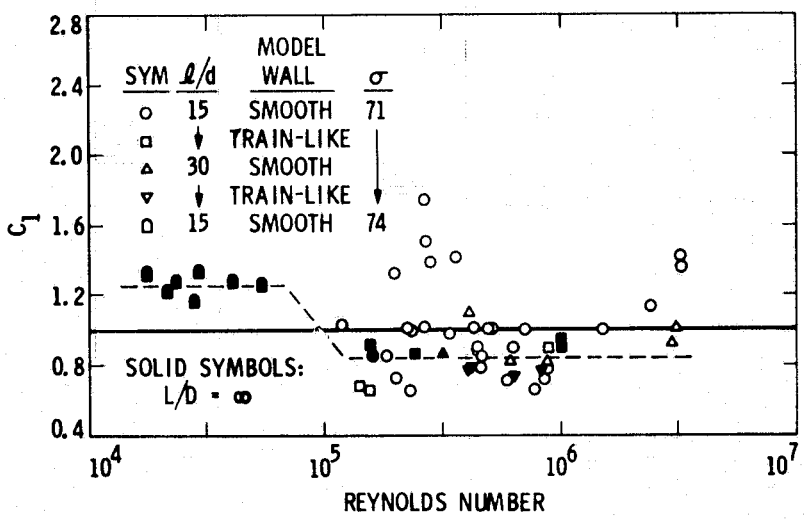

Fig. 13. Effect of Reynolds number on nose momentum coefficient (smooth tube wall, L/D = 630)

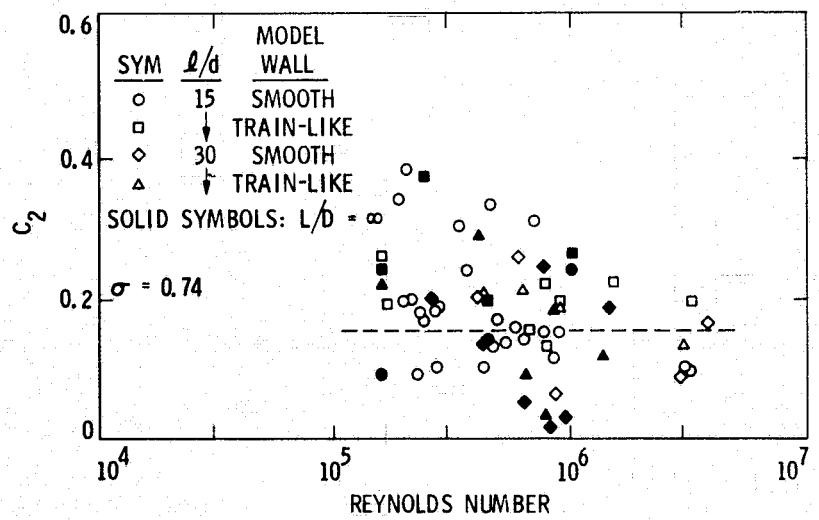

Fig. 14. Effect of Reynolds number on base momentum coefficient (smooth tube wall, L/D = 630)

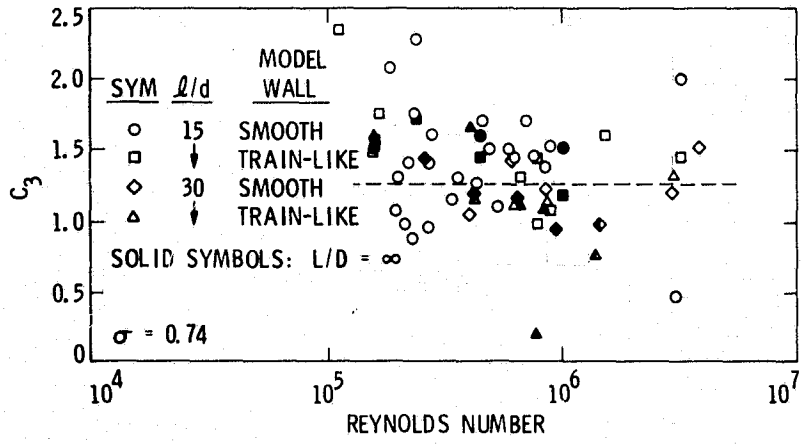

Fig. 15. Effect of Reynolds number on wake momentum coefficient (smooth tube wall, L/D = 630)

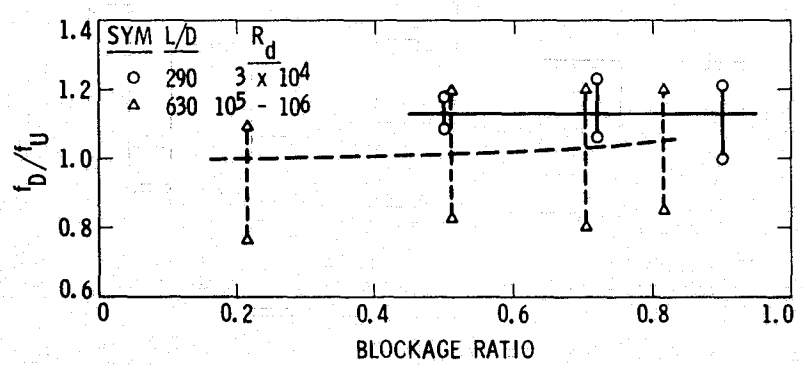

Fig. 16. Ratio of downstream to upstream pipe flow friction factors (smooth tube wall)

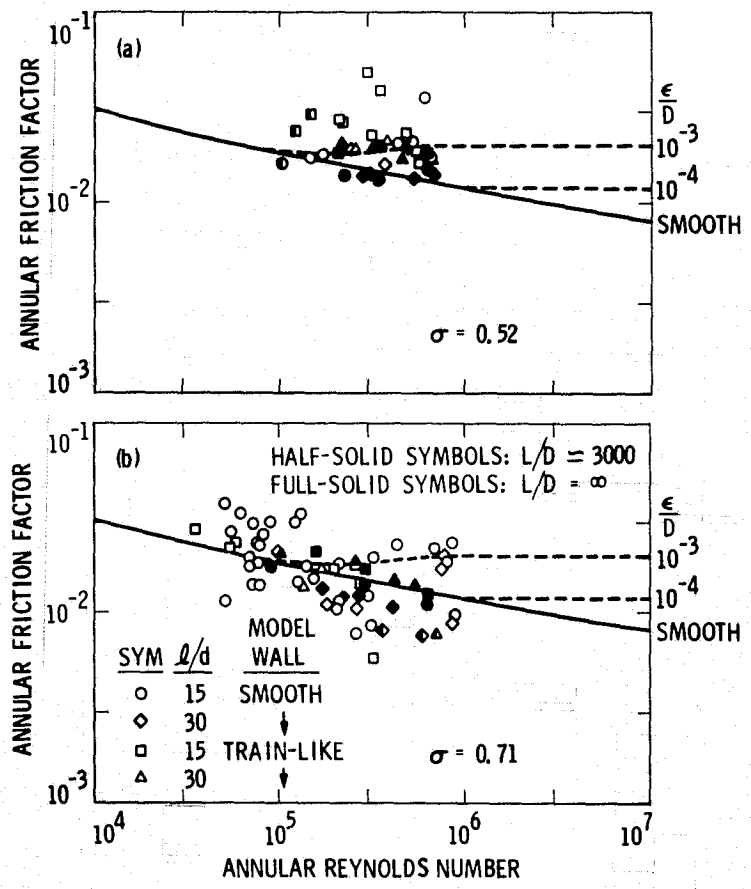

Fig. 17. Effect of annular Reynolds number on annular friction factor in a smooth wall tube (L/D = 630, ℓ/d = 15)

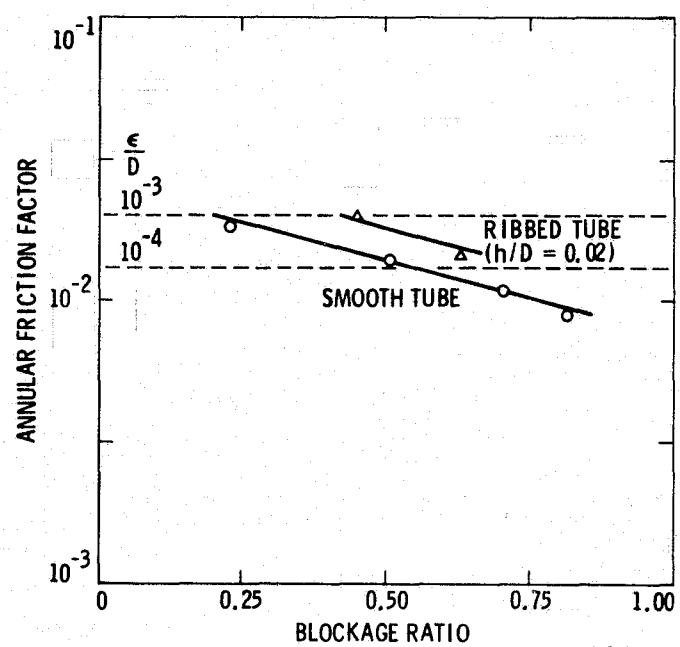

Fig. 18. Effect of vehicle blockage ratio on annular friction factor (annular Reynolds number = $1/2 \times 10^6$, smooth model wall, $\ell/d = 15$)

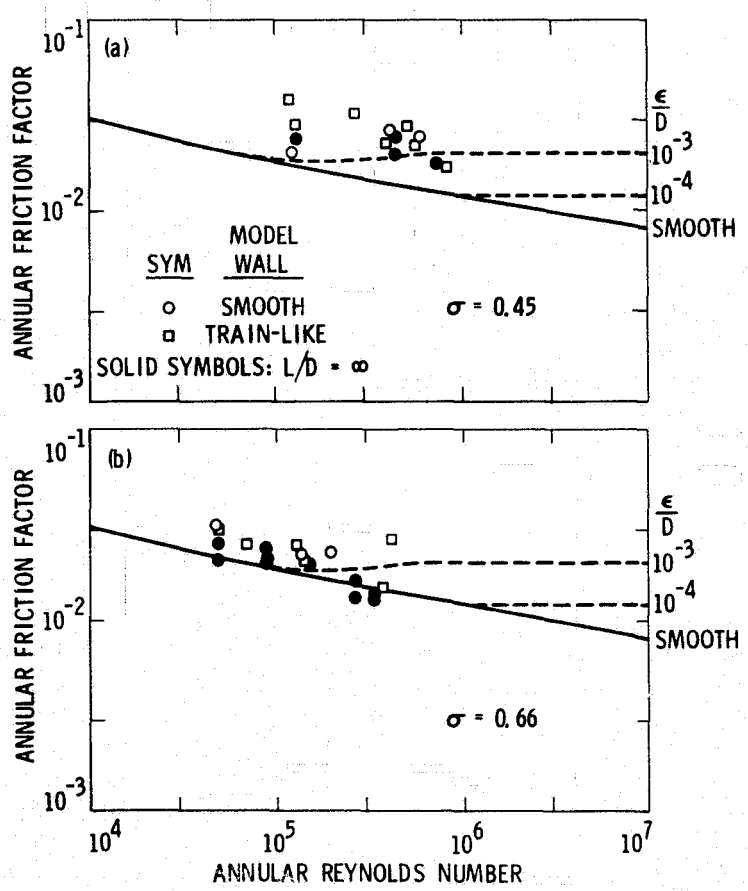

Fig. 19. Effect of annular Reynolds number on annular friction factor in a ribbed tube (L/D = 845, ℓ/d = 15)

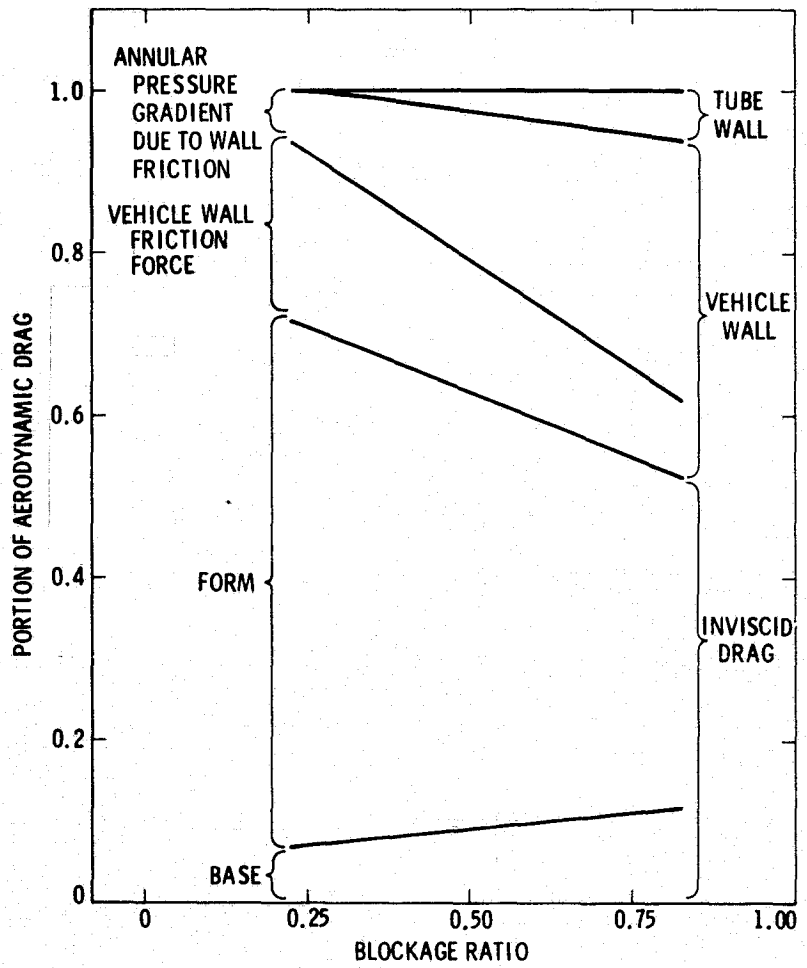

Fig. 20. Elements of aerodynamic drag ($R_d = 10^6$, all walls smooth, $L/D = 630$, $\ell/d = 15$)

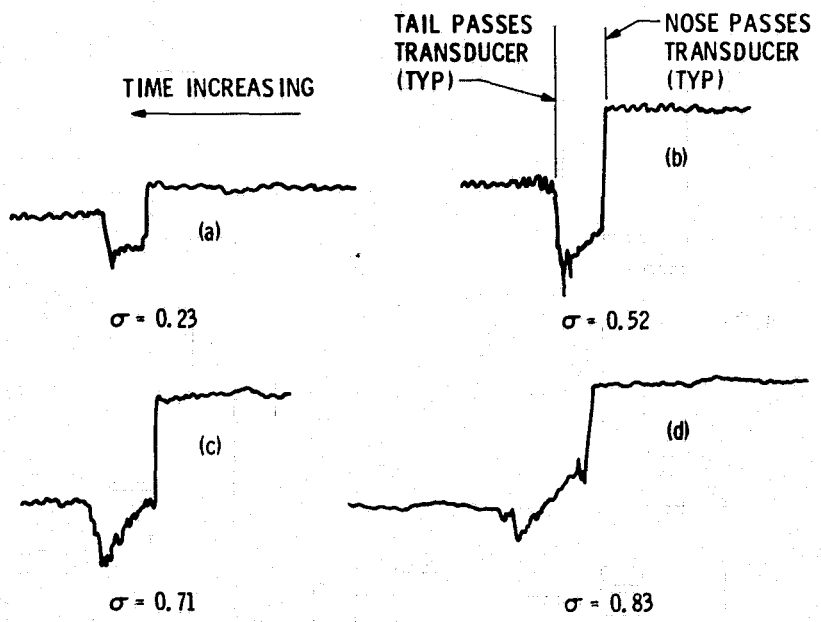

Fig. 21. Typical pressure signatures ($R_d \sim 3 \times 10^6$, all walls smooth, $L/D = 630$, $\ell/d = 15$)

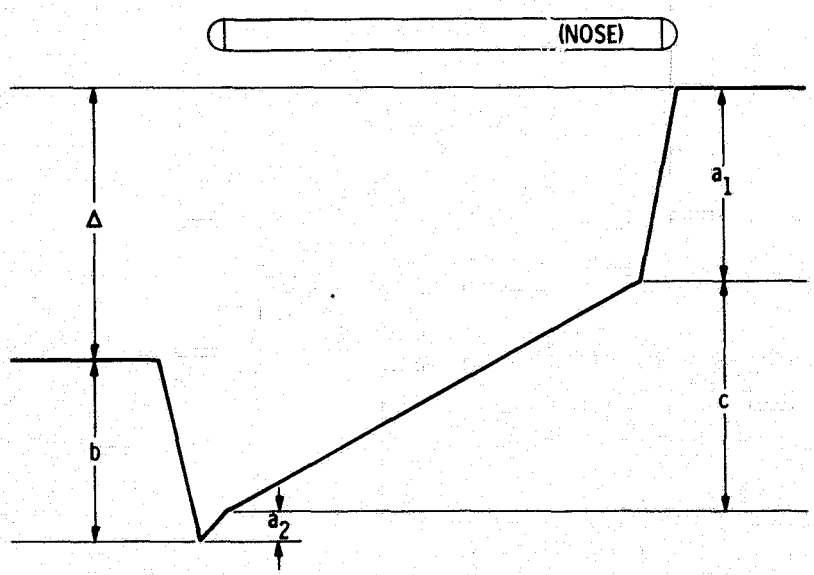

Fig. 22. Schematic of a typical pressure signature

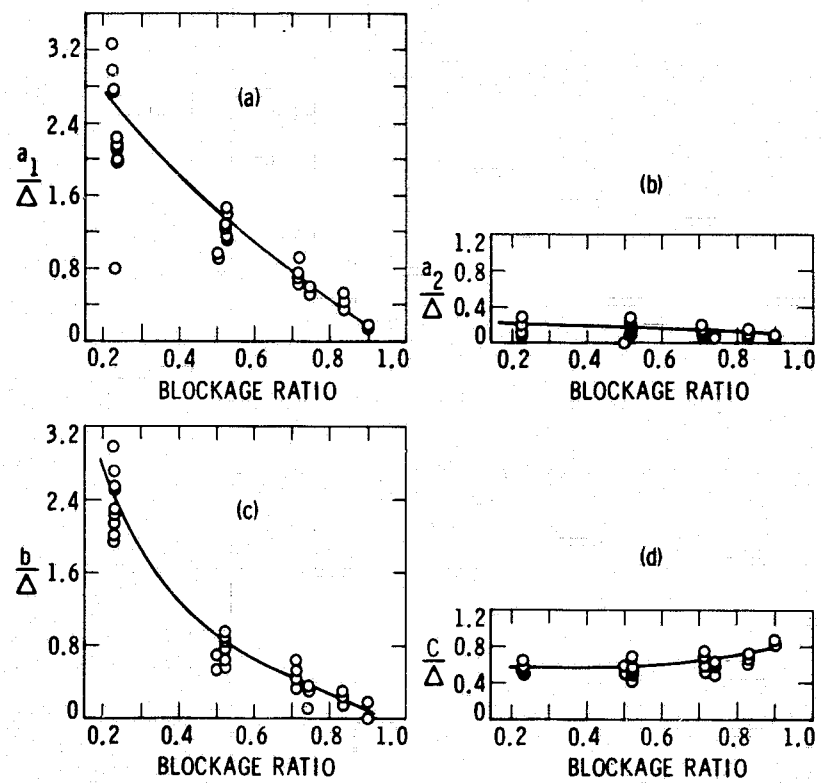

Fig. 23. Non-dimensionalized characteristics of typical pressure signatures

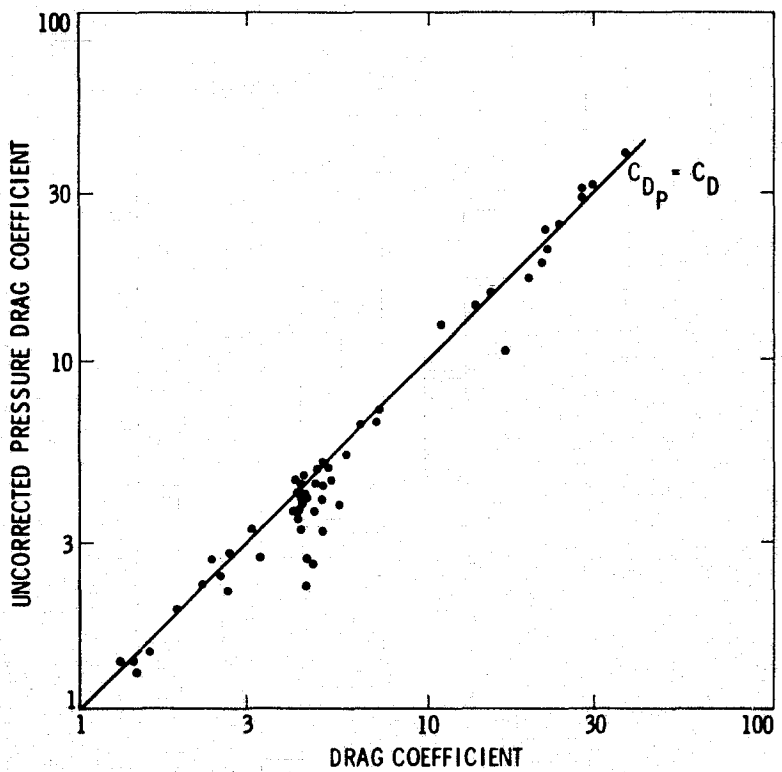

Fig. 24. Comparison of aerodynamic drag inferred from pressure signature with that directly obtained from model weight

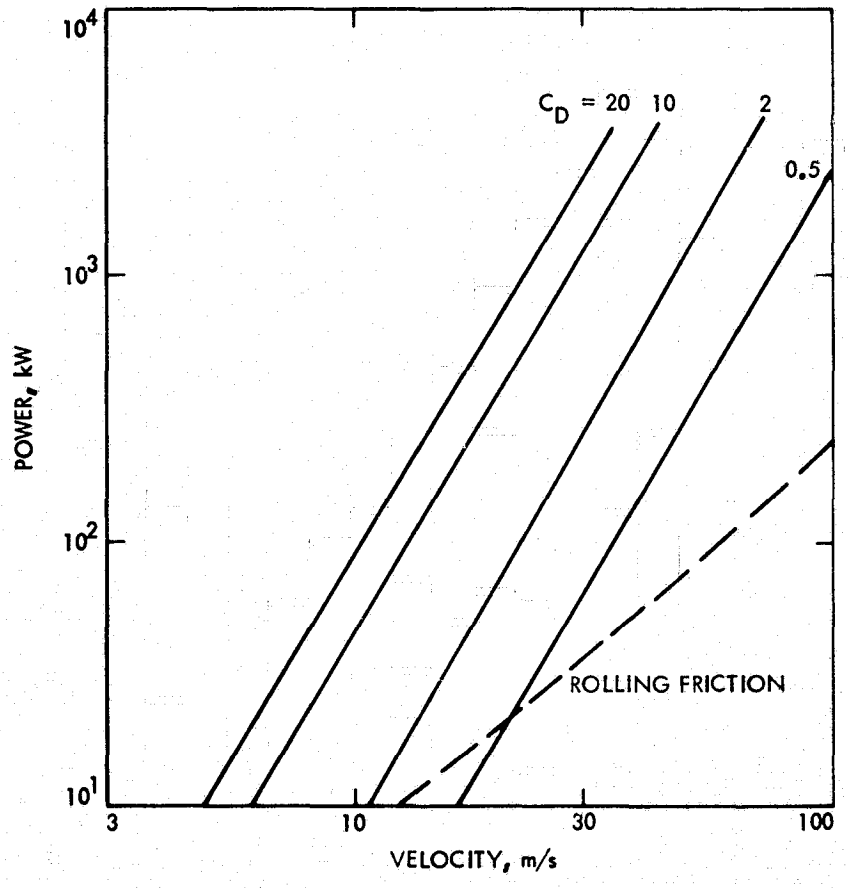

Fig. 25. Aerodynamic and rolling friction power requirement as a function of train velocity

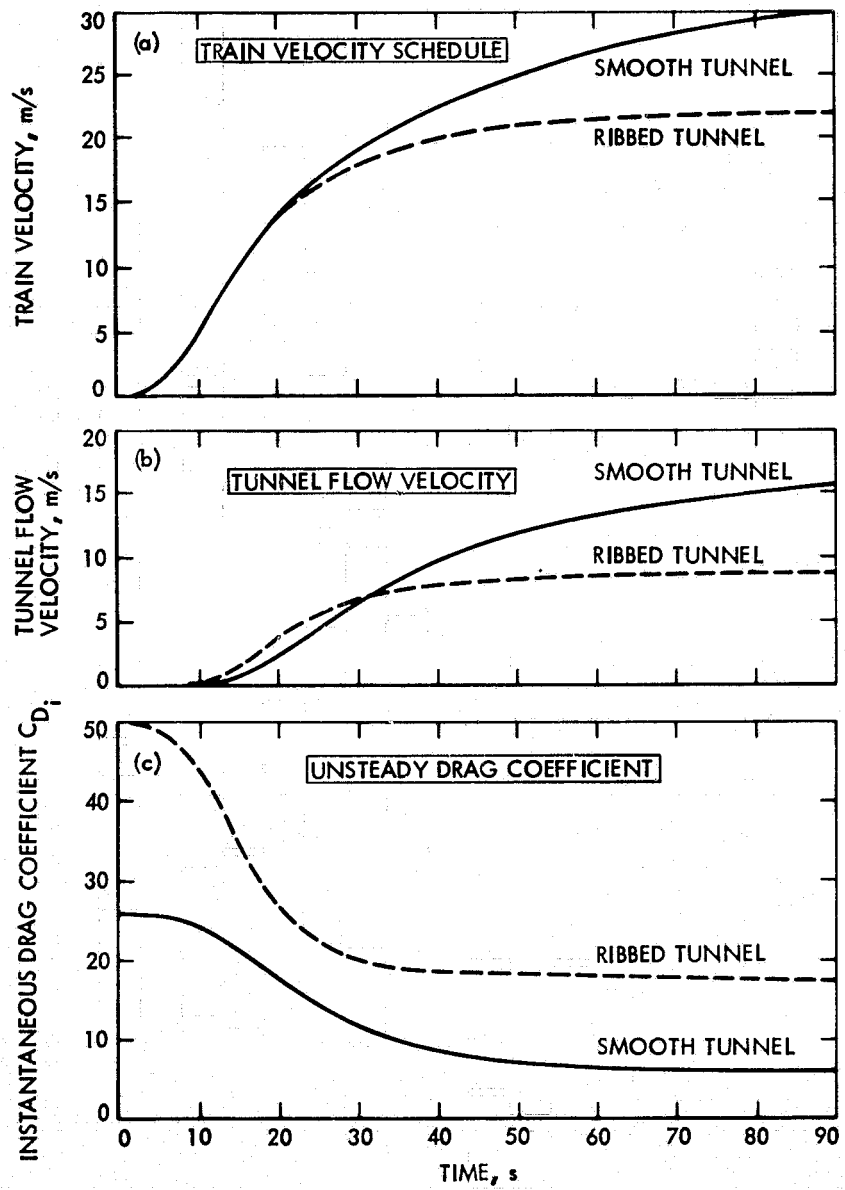

Fig. 26. Unsteady train velocity schedule, resulting air flow velocity in tunnel and instantaneous train drag coefficient

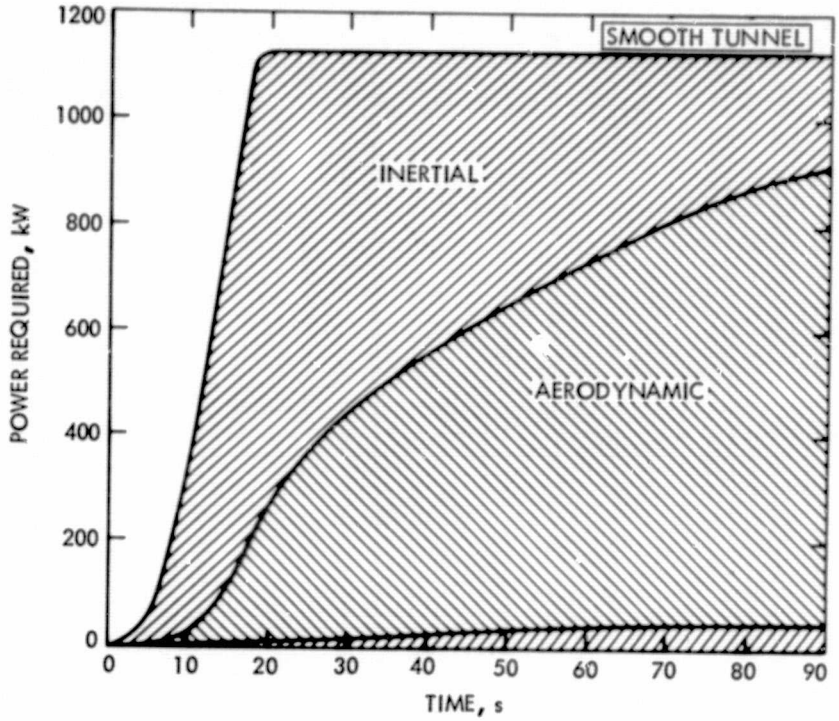

Fig. 27. Component parts of constant unsteady power requirement for train in a smooth tunnel

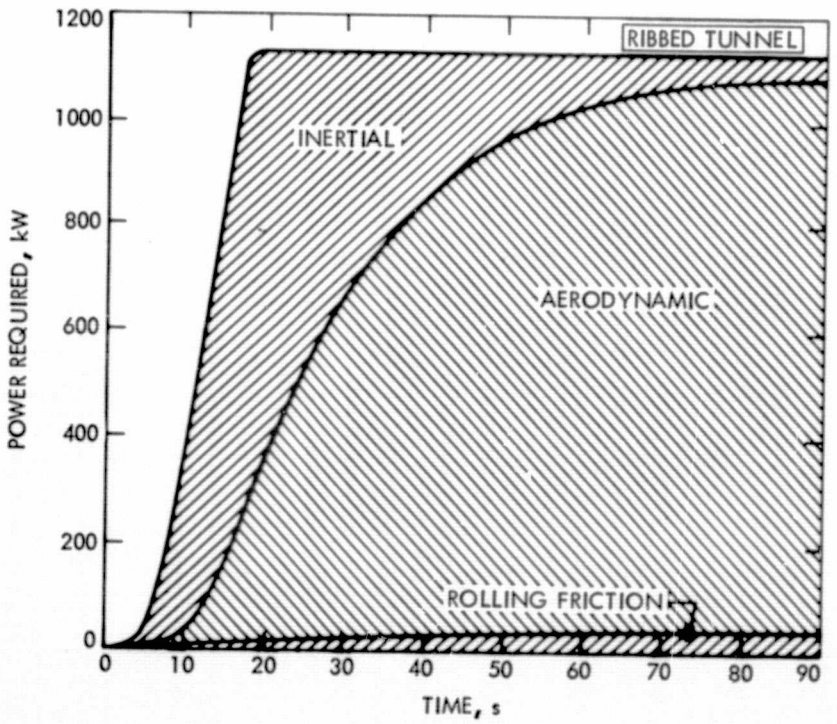

Fig. 28. Component parts of constant unsteady power requirement for train in a ribbed tunnel